JVST A
Journal of Vacuum Science & Technology A

Magnetron sputtered NiAl/TiB_x multilayer thin films

Cite as: J. Vac. Sci. Technol. A **40**, 033410 (2022); https://doi.org/10.1116/6.0001734
Submitted: 03 January 2022 • Accepted: 25 March 2022 • Published Online: 26 April 2022

Tomasz Wojcik, Vincent Ott, Sedat Özbilen, et al.

COLLECTIONS

Paper published as part of the special topic on Functional Coatings

View Online

Export Citation

CrossMark

ARTICLES YOU MAY BE INTERESTED IN

Systematic compositional analysis of sputter-deposited boron-containing thin films
Journal of Vacuum Science & Technology A **39**, 063408 (2021); https://doi.org/10.1116/6.0001234

Review Article: Stress in thin films and coatings: Current status, challenges, and prospects
Journal of Vacuum Science & Technology A **36**, 020801 (2018); https://doi.org/10.1116/1.5011790

Manipulation of thin metal film morphology on weakly interacting substrates via selective deployment of alloying species
Journal of Vacuum Science & Technology A **40**, 033407 (2022); https://doi.org/10.1116/6.0001700

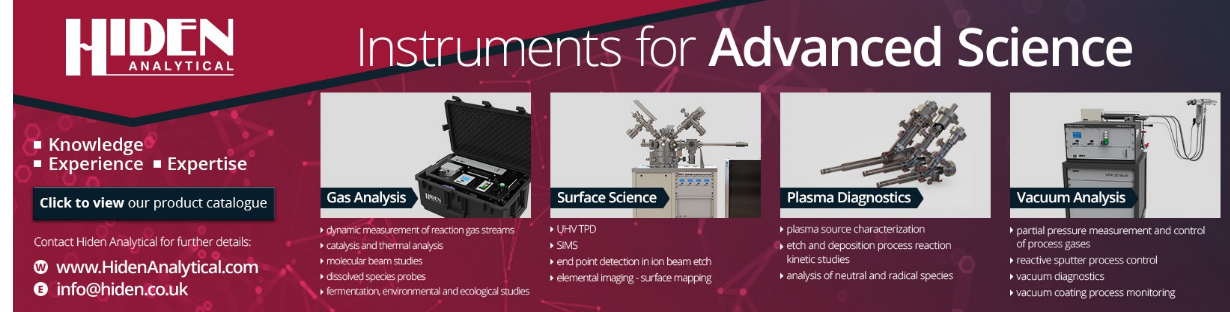

© 2022 Author(s).

ARTICLE

avs.scitation.org/journal/jva

Magnetron sputtered NiAl/TiB_x multilayer thin films

Cite as: J. Vac. Sci. Technol. A **40**, 033410 (2022); doi: 10.1116/6.0001734
Submitted: 3 January 2022 · Accepted: 25 March 2022 ·
Published Online: 26 April 2022

View Online

Export Citation

CrossMark

Tomasz Wojcik,[1] Vincent Ott,[2] Sedat Özbilen,[3] Harald Leiste,[2] Sven Ulrich,[2] Paul Heinz Mayrhofer,[1] Helmut Riedl,[1,a)] and Michael Stueber[2,b)]

AFFILIATIONS

[1]Institute of Materials Science and Technology, TU Wien, Getreidemarkt 9, 1060 Wien, Austria
[2]Karlsruhe Institute of Technology (KIT), Institute for Applied Materials (IAM-AWP), Hermann-von-Helmholtz-Platz 1, 76344 Eggenstein-Leopoldshafen, Germany
[3]Department of Mechanical, Manufacturing and Biomedical Engineering, Trinity College Dublin, University of Dublin, Dublin 2, D02 PN40, Ireland

Note: This paper is a part of the Special Topic Collection on Functional Coatings.
[a)]**Electronic mail:** helmut.riedl@tuwien.ac.at
[b)]**Author to whom correspondence should be addressed:** michael.stueber@kit.edu

ABSTRACT

Transition metal diboride-based thin films are currently receiving strong interest in fundamental and applied research. Multilayer thin films based on transition metal diborides are, however, not yet explored in detail. This study presents results on the constitution and microstructure of multilayer thin films composed of TiB_x and the intermetallic compound NiAl. Single layer NiAl and TiB_x and NiAl/TiB_x multilayer thin films with a variation of the individual layer thickness and bilayer period were deposited by D.C. and R.F. magnetron sputtering on silicon substrates. The impact of the operation mode of the sputtering targets on the microstructure of the thin films was investigated by detailed compositional and structural characterization. The NiAl single layer thin films showed an operation mode-dependent growth in a polycrystalline B2 CsCl structure with a cubic lattice with and without preferred orientation. The TiB_x single layer thin films exhibited an operation mode independent crystalline structure with a hexagonal lattice and a pronounced (001) texture. These TiB_x layers were significantly Ti-deficient and showed B-excess, resulting in stoichiometry in the range $TiB_{2.64}$–$TiB_{2.72}$. Both thin film materials were deposited in a regime corresponding with zone 1 or zone T in the structure zone model of Thornton. Transmission electron microscopy studies revealed, however, very homogeneous, dense thin-film microstructures, as well as the existence of dislocation lines in both materials. In the multilayer stacks with various microscale and nanoscale designs, the TiB_x layers grew in a similar microstructure with (001) texture, while the NiAl layers were polycrystalline without preferred orientation in microscale design and tended to grow polycrystalline with (211) preferred orientation in nanoscale designs. The dislocation densities at the NiAl/TiB_x phase boundaries changed with the multilayer design, suggesting more smooth interfaces for multilayers with microscale design and more disturbed, strained interfaces in multilayers with nanoscale design. In conclusion, the volume fraction of the two-layer materials, their grain size and crystalline structure, and the nature of the interfaces have an impact on the dislocation density and ability to form dislocations in these NiAl/TiB_x-based multilayer structures.

Published under an exclusive license by the AVS. https://doi.org/10.1116/6.0001734

I. INTRODUCTION

Advanced engineering thin film materials for applications under severe conditions and high loads require complex, multifunctional properties profiles including high strength, ductility, fracture toughness, oxidation, corrosion, and wear resistance.[1–4] Strong concepts for the development of novel materials for such challenging applications are explored in research. Exemplary, innovative nanostructured composite[5–7] and nanoscale multilayer[8–12] thin films (combining metals, metallic, and ceramic hard materials in multiphase structures) have been achieved by materials design on the atomistic level through tailored alloying,[13,14] interface modification,[13,15] and further strategies,[16,17] based on a deep understanding of plasma-based thin film growth,[18] materials simulation

Published under an exclusive license by the AVS

and modeling,[19–21] and fostered by the emergence of new deposition technologies like high-power impulse magnetron sputtering (HIPIMS).[22]

This work describes a new model case of magnetron sputtered composite thin films, combining an intermetallic material, NiAl, and a ceramic-like hard material, TiB_2, in the form of nanoscale multilayers. The study presents detailed results on the constitution and microstructure of these multilayer thin films (and on the related single layer thin films, respectively). A motivation for this work is derived from the background of bulk TiB_2 reinforced metal matrix composite materials, which are known for promising mechanical properties in combination with good thermal and electric conductivity.[23–25]

The intermetallic compound NiAl is an interesting candidate material for high-temperature applications. Its properties are strongly related to its structure and strong covalent bonds between the nearest neighbor Ni and Al atoms. NiAl crystallizes in a B2 CsCl structure (space group Pm$\bar{3}$m, space group No. 221) with a cubic lattice, consisting of two interpenetrating cubic primitive sublattices. In this ordered structure, each Al atom is surrounded exclusively by Ni atoms and vice versa. A detailed understanding of the structure of NiAl and its physical, chemical, and thermodynamical properties has been achieved in past decades. The attractive properties' profile covers a high melting temperature (1676 °C), low density (5.95 g/cm^3), a good oxidation resistance at 1100–1400 °C with the ability to form a protective Al_2O_3 surface layer, and a high electrical and thermal conductivity. NiAl shows anisotropic elastic and plastic properties, and the properties can be tuned through a variable defect structure by vacancy design. A disadvantage is its brittle behavior at room temperature, hindering its processing and use as a bulk material for engineering applications.[26–29] The exploration of NiAl as a coating or thin-film material has been addressed by thermal spray, pack cementation, and other techniques since the first experiments based on magnetron sputtering methods date back to the 1990s.[30–33] For example, Ding *et al.*[30] demonstrated the formation of equiatomic single-phase B2 structured NiAl thin films by R.F. magnetron sputtering of a composite elemental target. Depending on the applied substrate material, these thin films were grown with a different crystallographic orientation and texture. NiAl thin films deposited on amorphous glass substrates showed a strong texture in (111) orientation, while thin films deposited onto aluminum substrates grew in a polycrystalline structure without preferred orientation. Similar results were reported by de Almeida *et al.*[31] for R.F. magnetron sputtered NiAl thin films using an intermetallic target of equiatomic concentration, 50 at. % Ni and 50 at. % Al. This study described the growth of equiatomic single-phase B2 structured NiAl thin films on (100) oriented Si and (110) oriented Ni substrates in dependence on the R.F. target power and the substrate temperature and correlated the observed microstructure formation strongly with these substrate and deposition conditions. The deposition of NiAl thin films by D.C. magnetron sputtering was investigated by Bestor *et al.*[32] revealing single-phase thin films grown with a (110) texture on Ni-base superalloy substrates.

Titanium diboride, TiB_2, is one of the technically most relevant borides for engineering materials. Due to its high strength and hardness (in the range of 27–30 GPa), its low density (4.5 g/cm^3) and high melting point (3225 °C), its good thermal and electrical conductivity, and its thermodynamical stability, it is particularly attractive for both bulk materials and protective coatings for tribologically stressed components as well as for ultrahigh-temperature applications. TiB_2 crystallizes in a hexagonal structure of the AlB_2-type (space group P6/mmm, space group No. 191) with a hexagonal lattice. This structure consists of periodically stacked, alternating Ti and B layers and exhibits strong ionic Ti–B and covalent B–B bonds.[34–36] In the Ti–B phase diagram, the TiB_2 phase shows a narrow single-phase width within a concentration of 65.5–66.7 at. % boron.[37]

The exploration and utilization of TiB_2 (and other transition metal diborides) coatings and thin films have been stimulating fundamental and application-oriented research for decades, addressing chemical vapor deposition,[38–42] physical vapor deposition (PVD),[43–46] including, for example, ion beam assisted deposition,[47] magnetron sputtering,[48–51] arc evaporation,[52] and further synthesis methods.[53] In the following, the focus is on magnetron sputtering synthesis of transition metal diborides only, as this field has seen enormous innovation and progress through the development and implementation of new pulsed deposition techniques like pulsed DC magnetron sputtering,[49,54–56] HIPIMS,[57–61] and combined DC magnetron sputtering and HIPIMS processes.[62,63] Further progress in transition metal diboride thin films development and processing is available through advanced simulation and modeling (for an introduction please see exemplarily Refs. 64–67). Advanced thin film design concepts, for example, alloying of the diborides with aluminum to improve their oxidation resistance and age hardening behavior,[68–73] and other ternary[74–77] or multielemental diboride thin films,[78,79] either in novel solid solution or core-shell structure[80] are briefly mentioned but not described in detail. A recently published, comprehensive review article by Magnuson *et al.*[81] provides deep, extensive insight into the diboride (and other) thin films synthesis, microstructure, their underlying physics and chemistry, and many issues of more relevance to better understand this class of materials and the correlation of their atomistic design with macroscopic properties.

The physical vapor deposition of transition metal diboride thin films is usually facing the challenge of achieving thin films with desired stoichiometry, i.e., TMB_2 (TM: transition metal). Often, the reported composition of PVD TiB_2 (and other) thin films deviates significantly from the perfect metal:boron ratio and is commonly referred to as TiB_x with values for x mostly in the range of 1.4–3.5. The fundamental thin-film physics background on how to achieve perfect thin film stoichiometry in "conventional" magnetron sputtered diboride thin films has been outlined by Petrov *et al.*[46] The precise adjustment of the B:Ti concentration ratio is possible by applying external magnetic coils around the bulk plasma generated by unbalanced magnetrons, resulting in plasma confinement and an increase of the electron temperature in the bulk plasma. This causes enhanced ionization of the sputtered species, both Ti and B, and enables the control and adjustment of the diborides thin films' stoichiometries because the ions can be attracted to the substrate with adjustable energy and flux ratio. Significantly increased metal ionization and plasma densities are available in HIPIMS.[82] Greczyinski *et al.*[22] recently reviewed fundamental aspects of HIPIMS processes and discussed their utilization for precise composition and microstructure control of various

Published under an exclusive license by the AVS

refractory hard coatings. They pointed out the huge potential of this new technique for knowledge-based thin-film design by exploring the new toolbox offered by complete process control and steering via ionized plasma species. This has been demonstrated for TiB_2 thin films by Bakhit *et al.*[59] The authors showed that proper adjusting of the pulse width has a strong impact on the peak current density, the electron density in the plasma, and the ionization of sputtered species. This parameter variation could be used to tune the TiB_2 thin-film stoichiometry, changing from slightly over-stoichiometric, $TiB_{2.08}$, to perfectly stoichiometric, TiB_2, and even pronounced substoichiometric, $TiB_{1.83}$.

A major challenge in PVD diboride thin films processing, strongly related to the stoichiometry of the thin film, is the microstructure formation under such conditions (and when specific requests for substrate materials and temperatures must be additionally met). The adjustment and control of the microstructure and its correlation with macroscopic thin film properties are absolutely necessary for the development of novel hard and tough, oxidation resistant diboride thin films for higher temperature applications. Intense research has been and is devoted to this field as briefly outlined below. Mayrhofer *et al.*[45] presented a microstructural model for conventional magnetron sputtered over-stoichiometric TiB_2 thin films deposited at low substrate temperature (300 °C). A crystalline (001) oriented TiB_2 phase with nanocolumnar grains is surrounded by a thin, less-ordered boron-rich tissue phase. This microstructure is thermally stable up to 700 °C annealing and is highly cohesive. Such conventional magnetron sputtered over-stoichiometric TiB_2 thin films were frequently reported to exhibit very high hardness values, often up to 40 GPa and higher. Mayrhofer *et al.* related the high hardness values with this special nanoscale microstructure, which should suppress dislocation nucleation and glide as well as grain boundary sliding during mechanical loading in hardness evaluation in nanoindentation. This microstructural model was supported by a combined experimental and simulation study by Kalfagiannis *et al.*,[64] suggesting that excess boron can be located both at interstitial sites of the hexagonal Ti layers of the TiB_2 lattice and at the grain boundaries of the (001) oriented TiB_2 grains. Recent reports on the microstructure of over-stoichiometric TiB_2 HIPIMS thin films by Nedfors *et al.*[58] and Bakhit *et al.*[73] confirm this basic model further, showing an amorphous boron-rich grain boundary phase surrounding a nanocrystalline, (001) oriented TiB_2 phase. Nedfors *et al.*[51] described the growth of stoichiometric TiB_2 thin films by D.C. magnetron sputtering at higher gas pressure and with modified magnetic field configuration, at 900 °C substrate temperature on alumina, resulting in a very dense, high-quality nanocrystalline TiB_2 microstructure with B-rich inclusions. Thörnberg *et al.*[63] reported on HIPIMS $TiB_{1.43}$ thin films with pronounced boron deficiency; these films were grown in a dense, columnar microstructure without columnar boundary phases and exhibited better oxidation performance in comparison to over-stoichiometric TiB_{2+x} thin films with significant boron excess, deposited by D.C. magnetron sputtering. Palisaitis *et al.*[83] presented a study based on detailed transmission electron microscopy analyses and simulation of a slightly B-deficient, substoichiometric $TiB_{1.9}$ thin film, deposited by unbalanced D.C. magnetron sputtering at 900 °C on alumina substrates. The epitaxial film of high crystalline quality showed planar defects in the TiB_2 lattice, and both model and experiment showed great coherence.

A well-established, powerful concept to design advanced engineering thin films with enhanced hardness, fracture toughness, wear resistance, and oxidation resistance is the multilayer approach.[8–11,15] In this context, the development of innovative PVD thin film materials based on transition metal diborides has been related to the combination of diborides with transition metal carbides, nitrides, and carbonitrides. Material combinations mainly of hexagonal TiB_2 and ZrB_2 layers and face-centered cubic TiC or ZrC,[84–86] TiN,[84,87] (Ti, Al)N, or (Zr, Al)N (Refs. 88–90) and related layer materials have found some interest, while there is much less work published in comparison to, for example, nitride and carbide PVD multilayers. Such coatings have been investigated with respect to their mechanical properties, wear behavior, and performance in tooling applications by systematic variation of bilayer periods, volume fraction and microstructure of the layer materials, and the phase boundary volume fraction. Noticeably, a thin film concept based on the combination of Ti–B–N and TiB_2 based layers and realized through chemical vapor deposition has found application in the tool industry (see exemplarily Ref. 91). For tribological applications, the combination of TiB_2 with other ceramic layers, both in a crystalline or amorphous structure, has also been reported. The ceramic layer materials include, for example, amorphous (diamond like) carbon,[92,93] boron nitride,[94] silicon nitride,[95] zirconia,[96] or others.[97] The combination of TiB_2 with metal layers has been addressed to accommodate high-stress levels in the ceramic layers with the intention to enhance the ductility and fracture toughness of such composite thin film materials. The relatively few research works available in this specific field cover both pure elemental and alloy layer materials, like Al,[98] Ti,[99,100] Cr,[101] Ni,[102] W,[103] or FeMn.[104] Wang *et al.*[104,105] suggested, for example, a phase transformation of a metastable cubic FeMn phase with f.c.c. lattice into a cubic phase with b.c.c. lattice under mechanical stress, which would contribute to enhanced fracture toughness of the TiB_2/FeMn multilayer composite structure. Reports on the combination of TiB_2 and intermetallic materials such as NiAl in multilayers are not yet published.

In this study, we present magnetron sputtered NiAl and TiB_x thin films as model materials to explore the combination of the intermetallic material NiAl and the metal-ceramic hard material TiB_2 in nanoscale multilayer NiAl/TiB_x thin films as a potential novel type of metal-TiB_2 composite thin films. The major focus of the work presented is on the characterization of phase composition and microstructure of the thin films. These were deposited as single layers and multilayers with a different mode of target operation, i.e., both R.F. and D.C. power was supplied to the sputtering targets, altering the plasma deposition conditions and growth of the layer materials. For the NiAl/TiB_x multilayer thin films, a variation of the individual layer thickness in the range of 50–500 nm was done to identify bulk volume and phase boundary effects on the growth of the layer materials under different targets operation modes.

II. EXPERIMENT

Single layer NiAl, TiB_x, and multilayer NiAl/TiB_x thin films were deposited by non-reactive magnetron sputtering processes

Published under an exclusive license by the AVS

with a Leybold Z 550 coater. The sputter unit was equipped with two power supplies for the sputtering targets, one D.C. and one R.F. power supply. A second R.F. power supply was used for plasma etching. Two sputtering targets, made of commercially available NiAl and TiB_2 plates (75 mm diameter, 6 mm thick), bonded onto water-cooled Cu holders with electrical power supply connections (Leybold PK 75 cathode), were placed in adjacent positions along a horizontal axis and were arranged in a 180° configuration. Substrate materials used in this study are single crystalline (100) oriented Si wafer pieces ($10 \times 10\,mm^2$) with a thin amorphous silicon oxide surface layer. The thin film deposition onto the substrates placed on a rotatable substrate table was done through a top-down process. The vertical distance between targets and substrates was 50 mm. All deposition processes described in this study were carried out without additional substrate heating with substrate temperatures in the range of 80–200 °C (the substrate temperature was determined in separate experiments by using a specific sample prepared with a calibrated thermocouple, connected with an electrical unit outside the vacuum chamber. These measurements were done only in stationary mode). The working gas used was argon at a constant pressure of 0.4 Pa during thin film deposition, while at 0.6 Pa during plasma etching and during sputter cleaning of the targets. The vacuum chamber was evacuated to a pressure up to 8×10^{-7} mbar (80 μPa) before the gas inlet. Prior to thin film deposition, the sputtering targets were sputter cleaned for 5 min at 250 W target power to remove potential surface contamination. Furthermore, the substrates were 15 min plasma etched at 800 W in an R.F. plasma discharge via the R.F. power supply at the substrate table to remove surface contamination and contribute to optimum thin film adhesion. These process steps were done with appropriate shuttering of both targets and substrates.

For the deposition of the NiAl layers, a commercial NiAl plate (FHR Anlagenbau GmbH, Germany, purity 3 N, stoichiometry: 50 at. % Ni and 50 at. % Al) was used as a sputtering target and operated in both D.C. and R.F. mode. To identify appropriate process parameters for the deposition of stoichiometric and crystalline NiAl thin films, two experimental series with a variation in the power applied to the target (100, 250, and 500 W) were realized. In one approach, the power on the target was supplied in D.C. mode, in another approach in R.F. mode. The substrate bias was 0 V (i.e., substrates were grounded) and the argon gas pressure was constant, 0.4 Pa, corresponding to an Ar gas flow of 46 SCCM. The thickness of the NiAl single layer coatings was in the range of 3.8–3.9 μm.

The selection of parameters for the deposition of the TiB_x layers was on the basis of the evaluation of the above described approach for NiAl thin film deposition, considering the subsequent sequential deposition of both layers in new NiAl/TiB_x multilayers and with respect to former research of the authors on magnetron sputtering of TiB_2 thin films.[45,106,107] A commercial TiB_2 plate (FHR Anlagenbau GmbH, Germany, purity 2N5) was used as a sputtering target and was operated again in D.C. and R.F. mode. In these experiments, the power applied to the TiB_2 target was 250 W, the argon gas pressure was 0.4 Pa, and the substrate bias was 0 V (i.e., the substrates were at ground potential). The single layer thin films had a thickness of ~5 μm.

NiAl/TiB_x multilayer thin films with a variation of the individual layer thickness and bilayer period were deposited via sequential layer deposition under the NiAl and TiB_2 targets by utilizing a stop-and-go mode of the substrate table rotation and an appropriate shutter movement (with a manual process control). This strategy for deposition was chosen to design multilayer thin films with various thicknesses of the individual layers and with chemically sharp interfaces between these layers. Two strategies for the multilayer processing were applied: in one case, the NiAl target was operated in R.F. mode and the TiB_2 target in D.C. mode, while in the second case, the NiAl target was operated in D.C. mode and the TiB_2 target in R.F. mode. The power supplied to the individual targets was 250 W, the argon gas pressure was 0.4 Pa, and the substrates were grounded (0 V bias). The first layer of the multilayer stack was always NiAl, and the second one (and always the top surface layer) was TiB_x. The overall thickness of all multilayer samples was 5–10 μm. The deposition conditions and architectural details of the NiAl/TiB_x multilayer thin films are summarized in Table I (please note that Table I shows the experimentally verified thickness values of the individual layer materials).

The thickness of the single layer thin films was determined via deposition on a Si substrate with part of the surface area covered by a polymer strip. After deposition, this strip was removed, and the remaining difference in surface heights was analyzed by a tactile surface profilometer (Tencor P-10). The measured data were used for the calculation of the thin films deposition rate in dependence on the applied process parameters. These values determined the deposition time of the samples under the respective sputtering target during the multilayer synthesis.

The elemental composition of the single layer thin films was analyzed through electron probe microanalysis (EPMA) with a Cameca Camebax Microbeam system and a Cameca SX 100 system. The electron beam was operated at 15 kV acceleration voltage and a 30 nA current. On each sample, three analyses were done on various surface areas. The reported compositional values are average values calculated from those individual ones. Data acquisition was made by wavelength dispersive x-ray spectroscopy, using various analyzer crystals (PET, PC2 und PC80) and standard samples as references (TiN, ArSi 10, TiC, YiG, AlFe-Rank, G12Ni, and TiB_2).

The surface topography and the morphology of the fracture cross section of selected thin film samples were examined by scanning electron microscopy (SEM) images. These images were made with a Zeiss Merlin microscope equipped with a Zeiss-GEMINI 2 system and with an FEI XL 30S FEG microscope. Various operational modes collecting either secondary electrons or backscattered

TABLE I. Deposition conditions and systematics of the NiAl/TiB_x multilayer thin films: target operation mode, individual layer thickness D, and bilayer period λ (target power 250 W).

Sample notation	NiAl mode	TiB_2 mode	D_{NiAl} (nm)	D_{TiB2} (nm)	λ (nm)
A	R.F.	D.C.	500	500	1000
B	D.C.	R.F.	500	500	1000
C	D.C.	R.F.	65	75	140
D	D.C.	R.F.	75	45	120

Published under an exclusive license by the AVS

electrons were used for SEM imaging. Prior to SEM analysis, the thin film samples were mounted on a special sample holder with an angle of 60° inclined versus the exciting electron beam, enabling imaging of both surface and cross-sectional morphologies of a sample simultaneously. The acceleration voltage of the electron beam was 15 kV with a current at the sample in the range 500 pA–3 nA.

Phase analysis and microstructure characterization were done by x-ray diffraction (XRD) measurements on a Seifert ID 3003 system in Bragg–Brentano geometry with Cu-K_α radiation ($\lambda = 1.540\,598$ Å, 40 kV, 30 mA). The step size of the measurement was 0.010° with a measuring time of 360 s per step. A Meteor 1D detector is used as a 1D line detector. The 2θ range covered in these measurements was 10°–90°. The assessment of the x-ray diffraction raw data is performed via the Highscore software using the ICCD PDF4+ database. Information on phase composition, crystallinity, crystalline structure, orientation, and texture formation was obtained. The data obtained from the x-ray diffraction analysis are corrected for $K_{\alpha 2}$ radiation using a Rachinger correction, and the background is subtracted from the measured data.

The microstructure was investigated in more detail by using transmission electron microscopy (TEM) on cross-sectional thin film samples on an FEI TECNAI F20, equipped with a field emission gun and operated at 200 kV acceleration voltage. TEM samples were cut, polished to a thickness of approximately 10 μm, and ion milled in a Gatan PIPS II. Bright-field (BF) overviews and dark-field (DF) micrographs reveal an insight into the microstructure, columns' morphology, and their size and growth direction. Selected area electron diffraction (SAED) patterns revealed the observed crystallites' crystal structure, orientation, and texture. Scanning TEM (STEM) images, captured by a high angle annular dark-field (HAADF) detector for mass contrast, show the element distribution of the coatings. Energy dispersive x-ray (EDX) and electron energy loss spectra (EELS) were acquired simultaneously for chemical analysis of heavy and light elements, respectively. The quantification of the EDX spectra was based on theoretically determined k-factors provided with the EDAX TEAM software. The B/Ti ratios were calculated out of EEL spectra and combined with the EDX quantification results of the other elements to get an accurate boron content. The oxygen content was obtained by EDX because the O-K edge overlaps with features of the Ti-L edge in EEL spectra. Since oxygen as a light element was quantified by EDX, these results are not as reliable as the metal to metal ratios.

III. RESULTS AND DISCUSSION

A. NiAl single layer thin films

The elemental composition of the magnetron sputtered NiAl single layer thin films deposited on Si wafer substrates with a variation of the target power and in dependence of the target operational modus is presented in Table II.

The NiAl thin films deposited in both R.F. and D.C. mode exhibit Ni and Al as major constituents and only low contamination by nitrogen, carbon, and argon (the sum of the atomic concentrations of these contaminations is about 2–3 at. % for all thin films). In the case of the R.F. magnetron sputtered NiAl thin films, the increase of the R.F. target power from 100 to 500 W results in a tiny shift of the concentrations of Ni and Al: the concentration of Ni increases from 46.0 to 49.2 at. %, while that of Al decreases from 52.2 to 48.6 at. %. However, these changes are all within the measurement accuracy. The Ni:Al concentration ratio increases from 0.88 for 100 W to 1 for 250 and 500 W. Concerning the results obtained for the thin films deposited with 250 and 500 W, the differences in their elemental concentrations are very small and are not further considered with respect to the number of analyses made per sample and the related standard deviations. The D.C. magnetron sputtered NiAl thin films show in all cases (independent of the D.C. target power) nearly identical elemental composition with equal atomic concentrations of both Ni and Al. It can be concluded that all NiAl thin films in this work exhibit a Ni:Al atomic concentration ratio of 1, and their compositions correspond with the stoichiometry of the sputtering NiAl target, 50 at. % Ni and 50 at. % Al. Thus, the NiAl single layer thin films exhibit a composition matching the stoichiometry of the B2 NiAl phase and its related phase field in the Ni–Al phase diagram,[29] and the reported results correspond with the literature on magnetron sputtered NiAl thin films.[30–33]

TABLE II. Elemental composition of magnetron sputtered single layer NiAl thin films deposited with a variation of power supplied to the sputtering target in R.F. and D.C. mode. The elemental composition was measured with EPMA.

	Ni (at. %)	Al (at. %)	C, N, and Ar (at. %)	Ni:Al
100 W R.F.	46.0	52.2	1.8	0.88
250 W R.F.	48.3	49.7	1.9	0.97
500 W R.F.	49.2	48.6	2.2	1.01
100 W D.C.	48.5	48.7	2.8	1.00
250 W D.C.	48.4	49.0	2.5	0.99
500 W D.C.	47.8	49.6	2.6	0.96

For the stoichiometric NiAl target, a sputter equilibrium is achieved after a short time, where exactly as many Ni as Al atoms are sputtered. Comparing the D.C. mode with the R.F. mode, more atoms are sputtered at the same target power in the D.C. mode because the energy of the argon ions is larger in the D.C. mode, and the sputter yield increases with the ion energy. In the D.C. mode, the cathode potential energy is −489 eV. The substrates are grounded and, thus, the anode potential energy is 0 eV. The plasma potential energy is about −20 eV and, therefore, between the cathode and anode potential. Then, the potential energy difference between plasma and target results in an average argon ion energy of 469 eV. In the R.F. mode, the cathode potential energy is −321 eV, and the plasma potential energy is +25 eV, resulting in an average argon ion energy of 346 eV. The substrates are also grounded in R.F. mode. Due to the self-bias effect, the plasma potential energy in R.F. mode is always higher than the target potential energy, i.e., the cathode potential energy, and the substrate potential energy, i.e., the anode potential energy. In previous work, the plasma potential was determined with an electric retarding field analyzer for different target materials used in magnetron sputtering. It has been shown that the plasma potential for conductive materials varies only slightly. This was demonstrated for magnetron sputtering of TiN and graphite, for example.[108] In this

Published under an exclusive license by the AVS

work, such considerations reflect the recorded values for the growth rate of 2 nm/s (120 nm/min) in D.C. mode and ∼1.5 nm/s (88 nm/min) in R.F. mode in the case of 250 W target power [and as well, exemplarily, the values for a deposition with 100 W target power, i.e., 0.66 nm/s (40 nm/min) in D.C. mode and ∼0.5 nm/s (32 nm/min) in R.F. mode].

The growth morphology and surface topography of NiAl single layer thin films deposited with a target power of 250 W on a Si wafer substrate by both R.F. and D.C. magnetron sputtering are shown in the SEM images in Fig. 1. These images are taken from fracture cross-sectional samples with the procedure outlined in Sec. II. Both NiAl thin films exhibit a fine-scale columnar morphology and a homogeneous cross-sectional microstructure without pronounced pores and growth defects on the microscale. Their surface topography is very homogeneous, smooth, and free of large-scale defects. The cross-sectional morphology and structure of the two NiAl thin films are similar, irrespective of the different deposition processes. With regard to the substrate temperature, the melting temperature of bulk NiAl, and the gas pressure of 0.4 Pa (3 mTorr), such thin film morphology is attributed to a region close to the transition region between zone 1 and zone T in the structure zone model of Thornton.[109] During a deposition in the D.C. mode, the substrate is bombarded with electrons because the plasma potential energy amounts to −20 eV and is negative with respect to the grounded substrate. The electrons have an average energy of 20 eV, and this leads to slight heating of the substrate and, thus, to slightly higher surface mobility during thin film growth. In the R.F. mode, the plasma potential energy is about 25 eV, so the mean argon ion energy is 25 eV. This low-energy ion bombardment also increases surface diffusion during film growth. This can explain why the film growth is comparable at the same target power and working gas pressure for the two different modes. The fracture behavior of both thin films is very similar, as indicated by the smooth fractured areas shown in Fig. 1.

Figure 2 presents the results of the phase and microstructure analyses obtained from x-ray diffraction for NiAl single layer thin films on Si wafer substrates. All measured XRD data were compared with the standardized data available in the ICDD database. The overall observation is that all deposited thin films are nanocrystalline and single-phase. The analyzed XRD reflections attributed to the NiAl thin films can all be assigned to the cubic AlNi phase as specified in the ICDD card No. 00-044-1188. Furthermore, the NiAl thin films deposited on Si wafer substrates in this study grow with a pronounced texture when deposited at high R.F. target power.

Figure 2(a) shows the impact of the R.F. target power on the phase composition and microstructure of the NiAl thin films. Independent of the XRD reflections of the Si wafer substrate (at a diffraction angle 2θ at 69.132°), all other measured XRD reflections are attributed to the cubic AlNi phase. The deposited thin films are, therefore, considered crystalline, single-phase AlNi (or, according to the more common nomination in literature, single-phase NiAl). Independent of the R.F. target power, the deposited thin films are polycrystalline as all XRD diagrams show reflections of various lattice planes of the AlNi phase, namely, of (110), (111), and (211) lattice planes. The measured diffraction intensities of these signals are, however, different and do not reflect the theoretically expected intensities distribution according to the ICDD card. This indicates the growth of the NiAl thin films with preferred orientation. Especially, the diffraction intensities of the (111) lattice planes are highest for all thin films. It should be noted that the absolute intensity of the (111) lattice planes is smaller in the case of the thin film deposited at 500 W R.F. target power in comparison to that of the thin film deposited at 250 W R.F. target power, which is attributed to a more pronounced inclination of the (111) grains versus the surface normal. Furthermore, the measured diffraction intensity of the (110) lattice planes is very low in all cases. A higher R.F. target power, resulting in a higher thin film growth rate, does not result in their more pronounced formation. On the other side, the diffraction intensities of the (211) lattice planes change with variation of the R.F. target power: this diffraction intensity is highest in the case of low R.F. target power, 100 W, and decreases clearly with increasing R.F. target power. This suggests that an increase of the R.F. target power to 250 and 500 W,

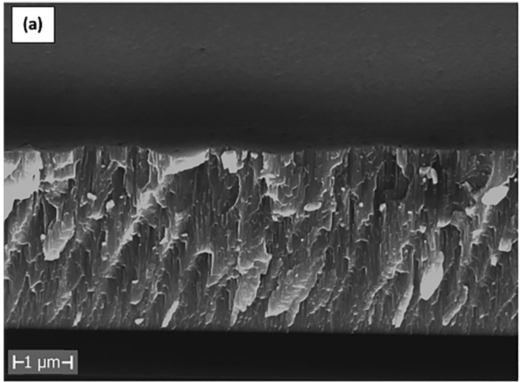

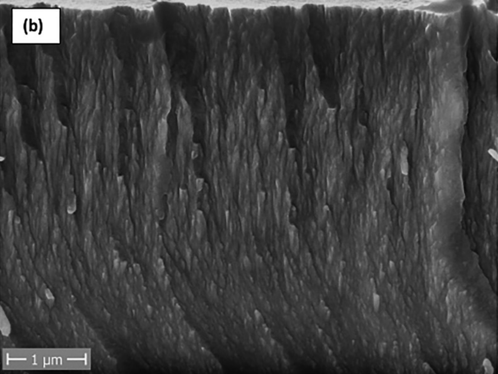

FIG. 1. Scanning electron microscopy images of the fracture cross sections of NiAl single layer thin films: (a) thin film deposited in R.F. mode at 10 000× magnification and (b) thin film deposited in D.C. mode at 20 000× magnification.

Published under an exclusive license by the AVS

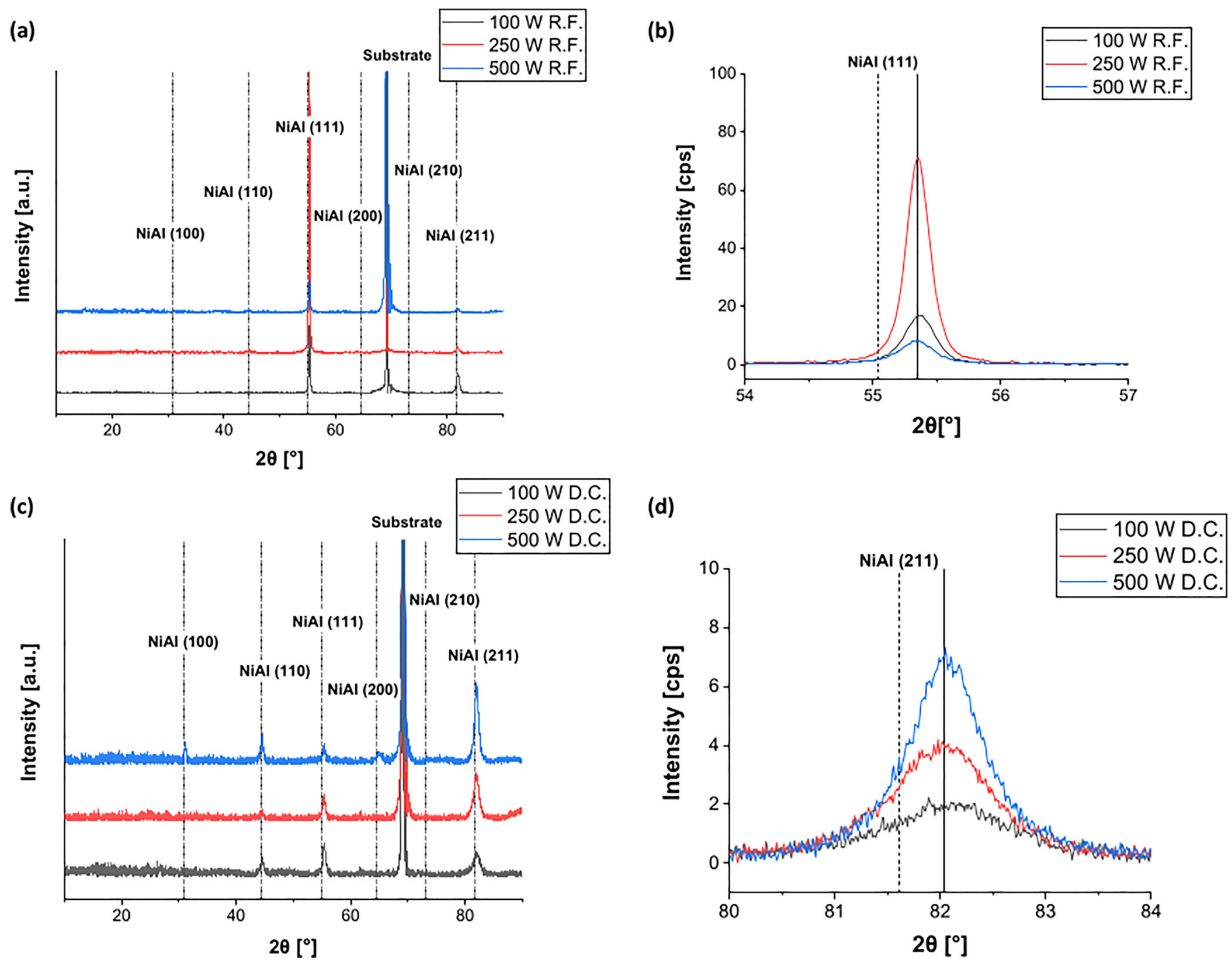

FIG. 2. XRD analyses in the Bragg–Brentano mode of magnetron sputtered NiAl thin films on Si wafer substrates in dependence of applied target power: (a) XRD patterns of R.F. magnetron sputtered thin films, (b) evolution of the (111) reflection of the R.F. magnetron sputtered thin films with applied target power, (c) XRD patterns of D.C. magnetron sputtered thin films, and (d) evolution of the (211) reflection of the D.C. magnetron sputtered thin films with applied target power. Dotted lines refer to the equilibrium positions of indicated lattice planes of B2 structured NiAl according to ICDD card No. 00-044-1188. The straight vertical line in (b) and (d) indicates (as a guide to the eye) the shift of the main diffraction reflection toward higher diffraction angles than specified in the ICDD card for the related equilibrium position.

respectively (while keeping the substrate bias voltage constant at 0 V and the argon gas pressure constant at 0.4 Pa), leads to a growth of these films with preferred (111) orientation. In the B2 CsCl structure, the most densely packed lattice plane is, however, the (110) plane not the (111) plane. Nevertheless, under the deposition and growth conditions applied in this work, the preferred atomic arrangement of the NiAl thin films appears in preferred growth with (111) oriented grains, especially at higher R.F. target power of 5.6–11.3 W/cm^2. This observation is very similar to results published, for example, by Ding *et al.*,[30] who deposited equiatomic, polycrystalline, and textured NiAl thin films with B2 structure by R.F. magnetron sputtering with 100–150 W R.F. target power (i.e., 5.1–7.6 W/cm^2, 80–150 °C substrate temperature, and 0.13–0.2 Pa argon gas pressure) at an argon gas pressure of 0.2 Pa on amorphous glass substrates. We used Si wafer substrates with an amorphous SiO_2 surface layer and obtained coherent results for the microstructure of the NiAl thin films. In the case of NiAl thin film deposition with 100 W R.F. target power (i.e., low deposition rate, low growth rate, and low rate of thin film-forming particles), the mobility of adatoms is limited, and the simultaneous growth of (211) oriented grains is observed, resulting in the formation of polycrystalline NiAl thin films. At higher R.F. target power, 250

Published under an exclusive license by the AVS

and 500 W (i.e., higher deposition rate, higher growth rate, higher rate of thin film forming particles, and thus, possibly slightly enhanced substrate temperature and enhanced surface diffusion of adatoms), the growth of NiAl thin films with preferred (111) orientation is energetically favored.

All XRD reflections are relatively sharp and exhibit values for the FWHM in the range of 0.2113°–0.3226° and are symmetric. A more detailed evaluation of the crystallite size on basis of the Debye–Scherrer formula is, however, not appropriate on this data basis. A very tiny shift of the diffraction signals to higher diffraction angles as specified for the theoretical position in the ICDD card can be seen in Fig. 2(a). This situation is illustrated in more detail in Fig. 2(b), showing an extract of the XRD data over a small 2θ angular range around the (111) orientation of AlNi. It is obvious that the XRD reflections of the NiAl thin films are indeed shifted by approximately 0.4° toward a higher diffraction angle, which is a little bit more pronounced in the case of the thin film deposited at the highest R.F. target power, 500 W. The estimation of the lattice constant *a* of the NiAl phase on the basis of all measured XRD reflections leads to a value of 0.2877 nm, identical for all three thin films and independent of the R.F. target power. These values are, however, smaller than the theoretical value of 0.2888 nm as specified in the ICDD card. This deviation can be correlated with the probably less dense thin film microstructure and with an impact of thin-film contamination as described above and would correspond with the existence of a tensile stress state in the films. This is in accordance with the cited structure zone model.

The XRD patterns of the D.C. magnetron sputtered NiAl thin films in dependence on the applied target power are shown in Fig. 2(c). Again, all XRD reflections attributed to the sputtered thin film reflections can be assigned to the cubic AlNi phase. The thin films are, thus, crystalline, single-phase NiAl. Independent of the applied D.C. target power, the thin films are polycrystalline. Their XRD patterns show reflections of various lattice planes of the NiAl phase, namely, of (100), (110), (111), (200), and (211) lattice planes. The measured diffraction intensities of these signals are again different and do not reflect the theoretically expected intensities distribution according to the ICDD card. This suggests a growth of these NiAl thin films with preferred (211) orientation, especially at higher D.C. target power. Indeed, the diffraction intensities of the (211) lattice planes increase clearly with increasing D.C. target power and are the highest of all recorded reflections. Different from the R.F. magnetron sputtered NiAl thin films, those deposited by D.C. magnetron sputtering exhibit in their XRD patterns reflections of the (110) lattice planes, but it is obviously (i.e., under the applied deposition and growth conditions) not the dominating or energetically most preferred lattice plane. The deposition at higher D.C. target power leads to a growth of these NiAl thin films in the preferred (211) orientation. The microstructures reported here for the D.C. magnetron sputtered thin films are in good agreement with those reported for D.C. magnetron sputtered pure NiAl and moderately (Hf) alloyed NiAl thin films.[32,110]

The XRD reflections of the D.C. magnetron sputtered thin films are broader compared to those of the R.F. magnetron sputtered thin films and exhibit values for the FWHM in the range of 0.7845°–1.2944° and are all symmetric. The FWHM values decrease with increasing applied D.C. target power. As the target power increases, the electron bombardment at the substrate increases in the D.C. mode because the charge carrier density increases and so does the electron saturation current density. Furthermore, more film-forming particles condense on the substrate per area and time, resulting in more heat of condensation per time. Both effects lead to a higher substrate temperature. The XRD reflections show a small shift toward higher diffraction angles (compared with the data in the related ICDD card). This is shown in more detail in Fig. 2(d), showing an extract of the XRD data over a small 2θ angular range around the (211) orientation of AlNi. The XRD reflections of the NiAl thin films are indeed shifted by approximately 0.5° toward a higher diffraction angle, independent of the applied D.C. target power. The lattice constant *a* of the NiAl phase is estimated on the basis of the measured (211) XRD reflections and is 0.2876 nm, constant for all three thin films, and independent of the D.C. target power. These values are again smaller than the theoretical values specified in the ICDD card and correspond again with the existence of a tensile stress state in the films, which is in agreement with the cited structure zone model again. The lattice parameter (and the elemental composition) of the magnetron sputtered NiAl thin films in this study is not affected by the operation mode of the sputtering target, while this has a significant impact on the crystalline structure, i.e., growth with a preferred orientation of these thin films.

Further details on the microstructure of the NiAl thin films are derived from transmission electron microscopy investigations of cross sections of thin films deposited on Si wafer substrates. Figure 3 shows exemplary results for a NiAl thin film deposited in the R.F. magnetron sputtering mode at 250 W. The BF image in Fig. 3(a) shows a very fine-scale, homogeneous, dense, and columnar microstructure over the entire thin-film cross section. The fine-scale columns show only very small, random tilting versus the surface normal vector, possibly a bit more pronounced in the interface zone close to the Si substrate. This can be associated with the nucleation and growth of the cubic (111) oriented NiAl phase on the amorphous SiO_2 layer on the Si wafer substrate, at a fast growth rate of ∼1.5 nm/s. Two selected areas for diffraction, one in a more surface-near region (b_I) and one close to the substrate (b_{II}) of the thin film, are marked by dashed white circles in the BF image. The SAED patterns for both regions are presented in Fig. 3(b). The upper part corresponds to the region b_I and the lower to b_{II}, respectively. These two SAED patterns are similar for both areas with a pronounced (110) ring and weaker (200) and (211) rings. The (111) is hardly visible, except at the top of the ring, which indicates the growth direction and is consistent with the XRD measurements. On the brightest (110) ring, locally accumulated intensities are strong evidence for texture. This texture appears more pronounced in the upper SAED than in the substrate-near one, where the intensity distribution over the ring is more smeared out with less distinct reflections. This fact is an indication of smaller column sizes close to the substrate.

The DF image in Fig. 3(c) is acquired on the (110) ring of the SAED pattern. The brighter areas represent the crystallites of the same orientation. Contrast inhomogeneities within the columns are caused by high densities of crystal defects and consequent local orientation changes inside the columns. We estimated an average

Published under an exclusive license by the AVS

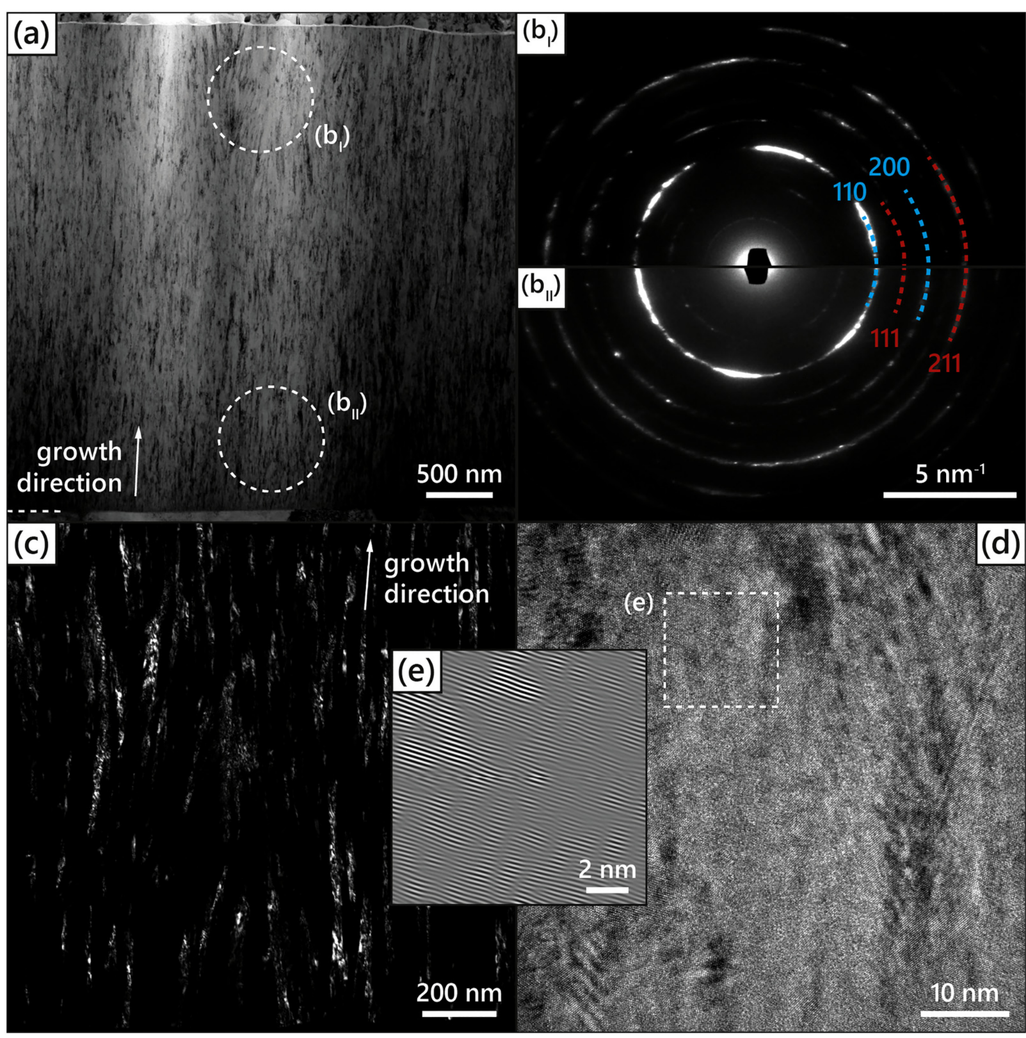

FIG. 3. TEM analysis of an R.F. magnetron sputtered NiAl thin film on Si wafer substrates after cross-sectional TEM sample preparation: (a) BF image with an indication of the thin film growth direction and the aperture positions used for electron diffraction in areas marked by dashed white circles, (b) SAED patterns of the two areas marked in (a), and indexing of major crystallographic orientations, (c) DF image, (d) HRTEM image, and (e) IFFT image of the area marked in (d) by white dashed lines.

column size of 23 ± 9 nm. Figure 3(d) presents a high-resolution TEM (HRTEM) image showing a larger column in the center of the image, which can be recognized by its homogeneous contrast values. There are well-aligned lattice fringes inside this grain with local inhomogeneities like crystal defects. In order to reveal the lattice fringes which are parallel to the interface, we transform the HRTEM image into reciprocal space (fast Fourier transformation, FFT). Similar to dark-field imaging, we mask the 011 reflections and apply an inverse FFT. The IFFT image in Fig. 3(e) reveals the lattice periodicity and coherency in bright contrast and crystal defects and strain fields in dark contrast values. Although we see an insight into one column here, the contrast is relatively dark because of a relatively high density of crystal defects like dislocations, which can be recognized directly in the IFFT image. The estimation of the lattice parameter *a* of the NiAl phase on the basis of the lattice plane distance evaluation with the HRTEM image leads to a value of 0.2877 nm and matches exactly the results of the XRD analyses.

B. TiB_x single layer thin films

TiB_x single layer thin films were magnetron-sputter deposited with a target power of 250 W, supplied in both D.C. and R.F. operation modes (at 0 V substrate bias and at an argon gas pressure of 0.4 Pa). The elemental composition of the TiB_x thin films deposited on Si wafer substrates is presented in Table III.

The TiB_x thin films exhibit Ti and B as major constituents and low contamination by nitrogen, carbon, oxygen, and argon

Published under an exclusive license by the AVS

TABLE III. Elemental composition of magnetron sputtered single layer TiB_x thin films deposited with a target power of 250 W, supplied in both R.F. and D.C. modes. The elemental composition was measured with EPMA.

	Ti (at. %)	B (at. %)	C, N, O, and Ar (at. %)	B/Ti	Notation
250 W R.F.	26.2	71.3	2.5	2.72	$TiB_{2.72}$
250 W D.C.	26.9	70.9	2.2	2.64	$TiB_{2.64}$

(the sum of these atomic concentrations is 2.2–2.5 at. %), independent of the target operation mode. The concentrations of titanium and boron are 26.2–26.9 and 70.9–71.3 at. %, respectively, leading to a B/Ti concentration ratio of 2.64 for D.C. magnetron sputtered thin films and 2.72 for R.F. magnetron sputtered thin films. In consequence, the TiB_x thin film composition is independent of the deposition process (under the conditions used in this work) and shows a significant deviation in stoichiometry in comparison to the theoretical values of bulk TiB_2 (and to the sputtering target). The thin films are precisely nominated $TiB_{2.64}$ and $TiB_{2.72}$ but are referred to as TiB_x in this paper (except of cases, when a special thin film is considered). More specific, the TiB_x thin films are significantly Ti-deficient and exhibit a moderate B-excess concentration. Such deviation from perfect stoichiometry in magnetron sputtered TiB_2 thin films has often been reported in the literature (as outlined in Refs. 4 and 111 and other references cited in this article) and has been related with specific magnetic field configurations used in magnetron sputtering processes.[46] The correlation between elemental composition and thin-film microstructure is discussed further in this section after the presentation of SEM, XRD, and TEM data.

Figure 4 presents the fracture cross-sectional SEM images of two TiB_x layer thin films deposited with a target power of 250 W (by both R.F. and D.C. magnetron sputtering) on Si wafer substrates. The morphologies of the cross-sectional areas and the surface topographies of both TiB_x thin films are very homogeneous and smooth. There is no indication of larger pores and growth defects, and columnar grains cannot be identified on this scale of imaging. The fracture cross-sectional areas are featureless and dense. The target operation mode obviously has no impact on the morphology of the fracture cross section. Both types of TiB_x thin films show an identical fracture behavior (in this undefined fracture situation). Regarding the substrate temperature, the melting temperature of TiB_2, and the gas pressure of 0.4 Pa (3 mTorr), the thin film morphology is again expected to be characteristic for a zone 1 structure of the structure zone model of Thornton.[109] However, this is not confirmed a priori by the SEM cross-sectional images.

Results of phase and microstructure analyses obtained from x-ray diffraction investigations on both D.C. and R.F. magnetron sputtered TiB_x single layer thin films on Si wafer substrates are summarized in Fig. 5. The recorded XRD data were compared with the standardized data available in the ICDD database. The general observation is that the deposited thin films are crystalline, single-phase, and strongly textured with (001) orientation. All XRD reflections attributed to the TiB_x thin films can be assigned to the hexagonal TiB_2 phase as specified in the ICDD card No. 00-035-0741. Such microstructure and thin-film growth in (001) orientation has been frequently reported for magnetron sputtered TiB_x thin films with pronounced over-stoichiometries and various B/Ti concentration ratios, especially for films deposited with conventional

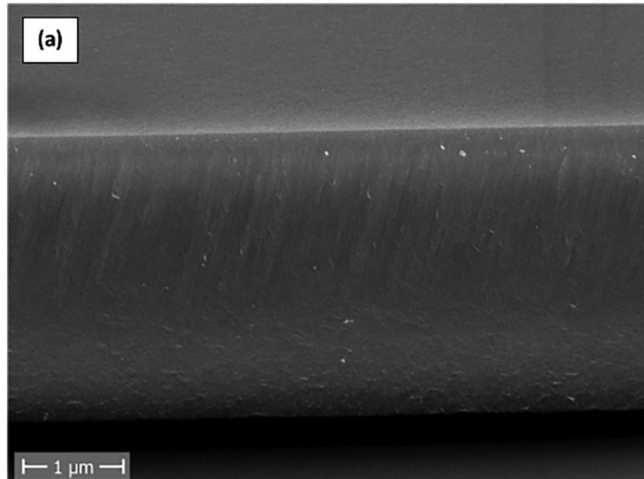

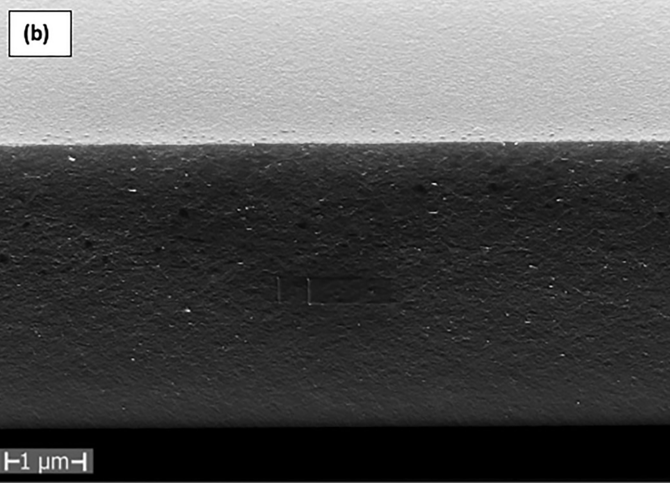

FIG. 4. Scanning electron microscopy images of the fracture cross sections of TiB_x single layer thin films deposited with a target power of 250 W: (a) $TiB_{2.72}$ thin film deposited in R.F. mode, 20 000× magnification and (b) $TiB_{2.64}$ thin film deposited in D.C. mode, 10 000× magnification.

Published under an exclusive license by the AVS

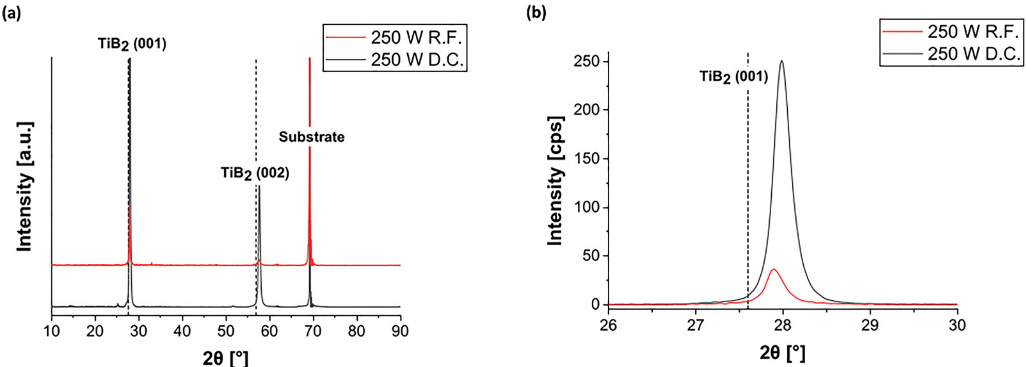

FIG. 5. XRD analyses in the Bragg–Brentano mode of magnetron sputtered TiB_x thin films on Si wafer substrates in dependence of the target operational mode: (a) overview of XRD patterns of R.F. and D.C. magnetron sputtered thin films and (b) evolution and shifting of the (001) reflection of the thin films with the changing target operation mode. Dotted lines refer to the equilibrium positions of indicated lattice planes of hexagonal TiB_2 according to ICDD card No. 00-035-0741.

magnetron configurations (see, for example, Refs. 4 and 111–113 and other references cited in this article).

Figure 5(a) shows the XRD patterns of the R.F. and D.C. magnetron sputtered thin films, shifted vertically along the *y* axis. XRD reflections of both the thin films and the Si wafer substrate are present in both cases. All reflections of the thin films can be assigned with the hexagonal TiB_2 structure, with (001) and (002) lattice planes, indicating a crystalline, single-phase, textured structure of both types of TiB_x thin films. The absolute intensities of the diffraction patterns are significantly higher for the D.C. magnetron sputtered thin films, which may be explained by a tilting of the grains versus the surface normal vector (as indicated below in the bright-field TEM image in Fig. 6). The (001) and (002) reflections are sharp and symmetric with FWHM values of 0.2308° and 0.2343° for the D.C. and R.F. magnetron sputtered thin films, respectively. Furthermore, the XRD reflections show a small shift to higher diffraction angles compared with the data in the related ICDD card [see Fig. 5(b)]. This shift is in the range of 0.4°–0.6° and is more pronounced in the case of the D.C. magnetron sputtered thin films. Due to the strong texture formation in both types of films, no statement is possible on lattice parameter *a*, and only lattice parameter *c* can be estimated. The values for *c* are 0.3198 nm in the case of the R.F. magnetron sputtered thin films and 0.3188 nm in case of the D.C. magnetron sputtered thin films. These values are smaller than the theoretical value specified in the ICDD card (0.3232 nm) and suggest a tensile stress state in both types of thin films. This corresponds with the above described Ti-deficient thin-film stoichiometries. Roughly speaking, the lattice parameter and the elemental composition of the magnetron sputtered TiB_x thin films in this study are not affected by the operation mode of the sputtering target, while this has some impact on the crystalline structure of these thin films.

The microstructure of the TiB_x thin films is further investigated by transmission electron microscopy. Figure 6 presents exemplarily results of the TEM analysis of a cross-sectional sample of a D.C. magnetron sputtered $TiB_{2.64}$ thin film on a Si wafer substrate.

The BF image [Fig. 6(a)] indicates a dense, homogeneous fine-scale columnar microstructure. The columns are well aligned from the interface to the substrate to the thin film surface, slightly tilted versus the substrate surface normal vector, and no intercolumnar voids or other features are visible. The area in the center of the thin film, marked with the dashed white circle, was chosen for TEM diffraction. The corresponding SAED pattern [Fig. 6(b)] shows pronounced, very sharp diffraction spots characteristic of a polycrystalline, strongly textured thin film microstructure with clearly aligned individual crystallites. The dominating diffraction spots stem from the (001) and (010) oriented lattice planes of the hexagonal TiB_2 crystal of space group P6/mmm [191]. These results are in agreement with the XRD results discussed above. Figure 6(c) shows a DF image, which confirms the dense, homogeneous fine-scale textured microstructure with well-aligned crystallites of identical orientation with an average size of 17 ± 5 nm. The HRTEM image [Fig. 6(d)] contributes to this interpretation in more detail. Over the entire area, the thin film exhibits a homogeneous, well-developed crystallinity with clearly defined and arranged lattice fringes of the hexagonal TiB_2 lattice. Various crystallites are visible, and the grain boundaries seem to be not amorphous. It can be seen that the grain boundary regions are somewhat disordered but two neighboring grains show pronounced orientation relations and lattice fringes extending across the grain boundaries. Figure 6(e) shows an IFFT image of the area marked by white dashed lines in Fig. 6(d), describing a TiB_2 crystallite and its neighboring areas. The IFFT image shows a perfect stacking of lattice fringes of the hexagonal TiB_2 lattice in bright contrast (view in the direction of the *c* axis of the hexagonal lattice) and boundary regions in darker contrast. In these dark regions, we can see dislocations, forming small-angle grain boundaries between the strongly textured columns. Without more advanced methods, we cannot further specify which element is represented by the bright and dark layers, but we point out the strong periodicity of the stacking sequence of these fringes in the center of the figure (we note explicitly, that deeper insight into the understanding of the nature of the grain boundaries would require further plan-view TEM

Published under an exclusive license by the AVS

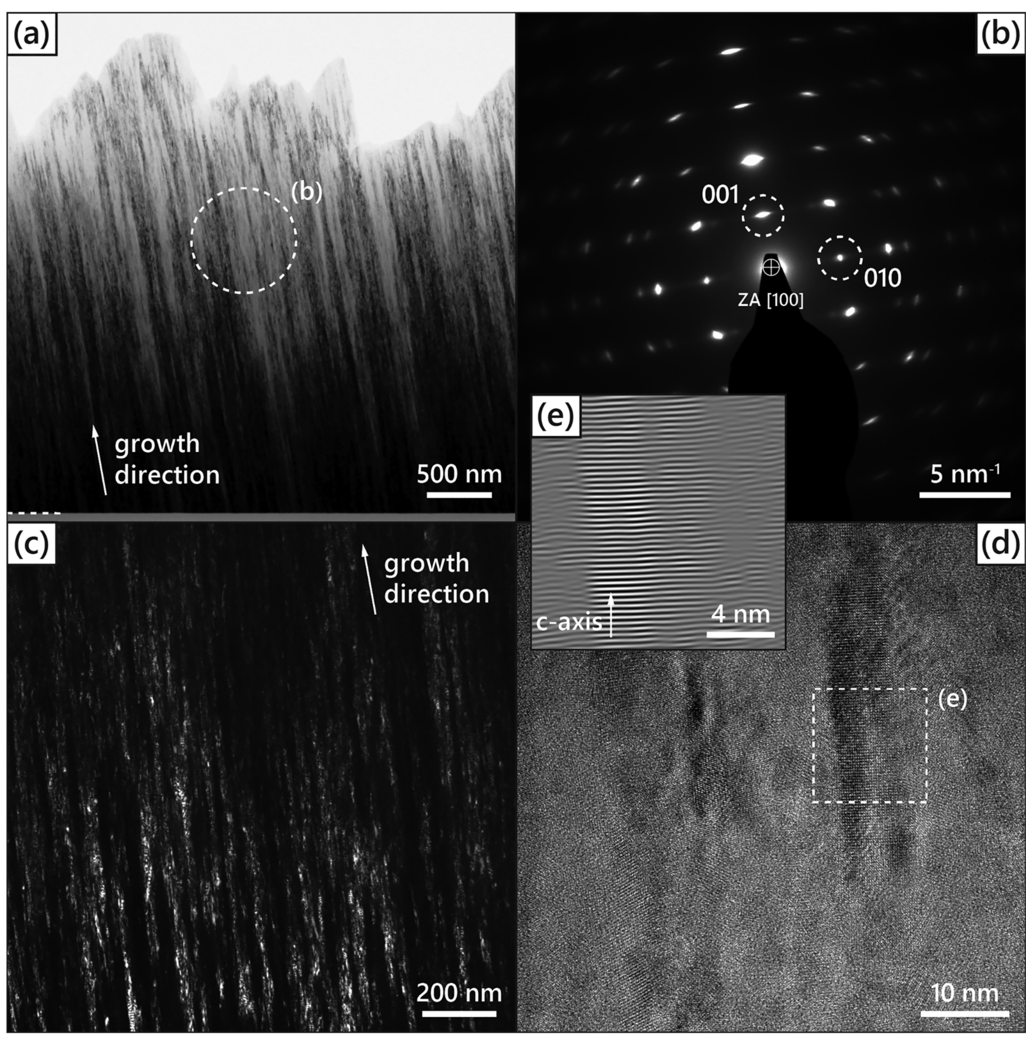

FIG. 6. TEM analysis of a D.C. magnetron sputtered $TiB_{2.64}$ thin film on Si wafer substrates after cross-sectional TEM sample preparation: (a) BF image with an indication of the thin film growth direction and the aperture position used for electron diffraction in the area marked by the dashed white circle, (b) SAED patterns of the area marked in (a), and indexing of major crystallographic reflections, (c) DF image, (d) HRTEM image, and (e) IFFT image of the area marked in (d) by white dashed lines.

investigations). The lattice parameter *c* can roughly be estimated from this image and is approximately 0.32 nm, which is very close to the theoretical value of TiB_2. This *c* axis value is slightly larger than the value derived from XRD data, but we should take into account that the column might not be perfectly aligned with respect to the electron beam, and we see only the projection of the lattice. Overall, we see a good agreement between the XRD and TEM data in this study.

Dislocations have only recently been reported in moderately substoichiometric $TiB_{1.9}$ thin films, deposited by unbalanced magnetron sputtering methods. Palisaitis *et al.*[83] explained the microstructure of such $TiB_{1.9}$ thin films with very high crystalline quality through the accommodation of their substoichiometry by the formation of stacking faults of the TiB_2 lattice. It should be noted that such high-quality thin films were deposited at 900 °C on alumina substrates, resulting in an epitaxial relationship between the substrate and $TiB_{1.9}$ thin films.[83] Thin films deposited at low substrate temperature and on other substrate materials, as in this study, exhibit a necessarily much higher degree of defects and disorder.[4,18] For conventional magnetron sputtered, significantly over-stoichiometric TiB_x thin films, Mayrhofer *et al.*[45] have suggested a structural model based on a crystalline TiB_2 phase surrounded by an amorphous-like boron-rich grain boundary phase. These two types of microstructures for TiB_x thin films (i.e., with and without pronounced grain boundaries phases and local atomic arrangement of the diboride crystal structure) will have a strong impact on the macroscopic thin film properties, for example, on mechanical properties and on deformation of these materials under mechanical

Published under an exclusive license by the AVS

loads, which has, for example, been demonstrated by Bakhit *et al.*[62] for diboride thin films in the Zr–Ta–B system by tailoring the thin film microstructure via described tools such as B/metal concentration, utilization of ionized and atomic species in pulsed deposition and further appropriate process and growth conditions. With respect to the discussed elemental composition and stoichiometry, the TiB_x thin films of this study should fit the structure model of Mayrhofer *et al.*[45] very well. The reported TEM results (Fig. 6), however, could suggest a structure more in between the two models, as a pronounced grain boundary phase and structure cannot be derived from the presented data. The Ti-deficiency of the TiB_x thin films is not unexpected for low-temperature deposition in conventional magnetron sputtering and under conditions applied in this study (i.e., low substrate temperature, no ion bombardment during film growth, target to substrate distance in the same order of magnitude as the mean free path length) and is in agreement with a detailed study carried out by Neidhardt *et al.*[50] This Ti-deficiency should correspond with vacancies in the hexagonal close-packed Ti planes of the TiB_2 lattice, while the moderate B-excess in the films would fit the Mayrhofer model (i.e., the existence of a B-rich grain boundary phase) but possibly not the simulations of Kalfagiannis *et al.*,[64] suggesting the possibility of excess boron at interstitial sites of the hexagonal Ti layers. Due to the textured microstructure of the discussed TiB_x thin films, lattice parameter a cannot be evaluated here, and lattice parameter c is only moderately smaller compared to the theoretical value of the stoichiometric, unstrained TiB_2 lattice. Consequently, a more precise statement on the existence and nature of a grain boundary phase in our thin films and on their microstructure would only be possible on the basis of additional TEM investigations of in-plane prepared samples and elemental analyses of such samples with high resolution.

C. NiAl/TiB_2 multilayer thin films

The multilayer thin films in this work were deposited by sequential deposition under the NiAl and TiB_2 sputtering targets by using an appropriate shutter technique and a substrate table movement in a stop-and-go modus with defined holding times under the respective targets. Both targets were powered with 250 W, both in D.C. and R.F. operation modes (while the argon gas pressure was 0.4 Pa, and the substrate bias was 0 V). The architecture of the NiAl/TiB_x multilayers was varied with regard of the individual layer thickness and the bilayer period. These architectures cover a microscale design (with an individual layer thickness of 500 nm for both NiAl and TiB_x layers) and as well two types of nanoscale designs. One is built upon NiAl and TiB_x layers with nearly equal individual thickness values in the range of 70 ± 5 nm, while the other refers to a multilayer design with a larger volume fraction of the pure metallic layer (NiAl) and a lower volume fraction of the ceramic-like layer, TiB_x. In the latter case, the thickness of the NiAl layer was chosen as 70 ± 5 nm, and that of the TiB_x layer was 50 ± 5 nm. This approach reflects the fact that microstructure formation and properties in multilayer thin films depend both on the volume fraction and microstructure of the constituent, individual phases, and materials (i.e., their grain and phase boundaries) and on the interface volume and design (i.e., atomic arrangement

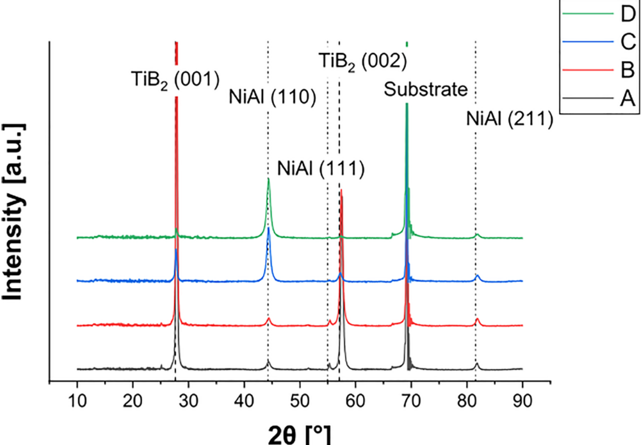

FIG. 7. XRD analyses in the Bragg–Brentano mode of magnetron sputtered NiAl/TiB_x multilayer thin films on Si wafer substrates in dependence of the deposition conditions and systematics outlined in Table I. Dotted lines refer to the equilibrium positions of indicated lattice planes of both cubic NiAl and hexagonal TiB_2 phases according to ICDD card Nos. 00-044-1188 and 00-035-0741 for AlNi and TiB_2, respectively.

at the interfaces). Nanoscale multilayers with appropriate design and combination of different layer materials should show enhanced ductility and reduced brittleness due to several effects: crack deflection, crack splitting, and dissipation of crack energy at interfaces. Especially, the interface, phase, and grain boundaries atomic arrangement will contribute to such advanced tough and durable PVD thin film materials. Furthermore, the potential impact of the target operation mode was addressed in this work by switching both the R.F. and D.C. supplies in an experiment on multilayer thin films with the largest bilayer period. The deposition conditions and design of the NiAl/TiB_x multilayer thin films are summarized in Sec. II, Table I.

Considering that the process parameters utilized for the multilayer thin film preparation are identical to those used for the synthesis of the single layer thin films, the individual layers of the multilayer thin films should grow in a microstructure very similar to the corresponding NiAl and TiB_x single layers. However, it has to be noted that (apart from the first layer of the multilayer composites) a NiAl layer is now always grown on a TiB_x layer, and a TiB_x layer is always grown on a NiAl layer. Thus, the microstructure formation and crystallographic orientation of the individual layers can be influenced by coherency strains and stresses forming at the respective interfaces and phase boundaries. The microstructure in general and the interfaces between the NiAl and TiB_x layers of the multilayer thin films are subsequently described by XRD and TEM investigations.

Figure 7 summarizes the results of phase and microstructure analyses obtained from XRD investigations for the multilayer thin films specified in Table I, deposited on Si wafer substrates. The XRD data were compared with the standardized data of the ICDD database as mentioned in Secs. III A and III B. Generally, the multilayer thin films are all crystalline and their diffraction patterns exhibit reflections that can be assigned to both NiAl and TiB_2

Published under an exclusive license by the AVS

phases according to the ICDD card Nos. 00-044-1188, and 00-035-0741, respectively.

First, we compare the multilayer thin films of type A and type B. In these cases, both layer materials have an individual thickness of 500 nm, resulting in a bilayer period of 1000 nm (and a NiAl:TiB_x layer thickness ratio of 1). The difference between the two multilayers is the operation mode of the NiAl and TiB_2 sputtering targets: for the deposition of multilayer type A, the NiAl target was operated in R.F. mode and the TiB_2 target in D.C. mode. This electrical circuit situation was reversely switched for the deposition of multilayer type B (i.e., the NiAl target was operated in D.C. mode and the TiB_2 target in R.F. mode). The XRD patterns of these multilayer thin films are very similar and show only minor differences in the intensities of the recorded diffraction reflections. The multilayer thin films are crystalline and consist of two phases. Diffraction reflections of both the AlNi and the TiB_2 phases are evident (according to the above specified ICDD cards). In the case of the titanium diboride, reflections of the (001) and (002) lattice planes are visible with high intensities. No other diffraction reflections are observed for the hexagonal TiB_2 structure. Like for the TiB_x single layer thin films, this speaks for a strong texturing of the microstructure of the TiB_x layers in the multilayer thin films. In the case of the intermetallic phase NiAl, reflections are observed for the (110), (111), and (211) lattice planes of the CsCl structure. Different from the observations made on the XRD patterns for the NiAl single layer thin films, reflections of the (111) lattice plane do not occur with the highest intensity in the multilayer thin films. In consequence, the AlNi layers in these two multilayer thin films are polycrystalline without a tendency to grow with preferred orientation. It can be further concluded that the target power configuration (and, thus, in a broader sense the plasma-physical conditions of the layer deposition) does not result in differences in the microstructure of these multilayer thin films.

Next, we compare the multilayer thin films, type B and type C. Now, both layer materials were deposited with identical target operation modes (i.e., the NiAl target was operated in D.C. mode and the TiB_2 target in R.F. mode). Multilayer thin-film type B has a nanoscale design with individual layer thickness values of 70 ± 5 nm for each layer material (which may still, roughly be considered as a NiAl:TiB_x layer thickness ratio of 1 and a bilayer period of 140 nm) and has, therefore, many more phase boundaries than the multilayer type A for identical multilayer thickness. The transition in multilayer architecture from the microscale (multilayer type B) to the nanoscale (multilayer type C) has a clear impact on the microstructure of the multilayer thin films. Again, the multilayer thin film type C is crystalline and consists of two phases, as indicated by diffraction reflections of both the AlNi and the TiB_2 phases. In the case of the titanium diboride, reflections of the (001) and (002) lattice planes are visible again but with significantly lower intensities as in the case of multilayer type B. However, these XRD reflections observed for multilayer type C are not shifted in their angular position while their FWHM values are slightly increased (compared to multilayer type B). Thus, the TiB_x layers in the nanoscale multilayer thin films grow with a tendency toward a textured microstructure. In the case of the NiAl phase, the x-ray diffraction patterns show diffraction reflections of the (110), (111), and (211) lattice planes of the CsCl structured NiAl. Thus, the NiAl layers in multilayer type C are polycrystalline, and the diffraction intensities of the (110) oriented crystallites are highest. This suggests that the growth of the NiAl layers in the nanoscale multilayers is also different from that observed for the microscale multilayers.

Finally, multilayers with designs, type C and type D, are compared. In this consideration, both layer materials were deposited again with the identical target operation mode (i.e., the NiAl target was operated in D.C. mode and the TiB_2 target in R.F. mode). Both multilayer thin films have a nanoscale design. According to Table I, multilayer thin-film type D has nearly the same NiAl layer thickness as multilayer thin film C, 75 nm, while the individual layer thickness of the TiB_x layer is reduced to 45 nm, resulting in a NiAl:TiB_x layer thickness ratio of 1.6 and a bilayer period of 120 nm. In consequence, the volume fraction of the TiB_2 phase in the multilayer stack is significantly reduced and the number of phase boundaries is increased in multilayer type D (compared to multilayer type C and for identical multilayer thickness). The x-ray diffraction patterns of the nanoscale multilayer thin film type D indicate again its crystalline, multiphase structure. Diffraction reflections of both NiAl and TiB_2 are recorded again. In the case of the titanium diboride, diffraction reflections of the (001) and (002) lattice planes of the hexagonal TiB_2 phase are observed, and the XRD patterns of multilayers type D and type C are very similar. There is no shift of these XRD reflections in their angular position, and their FWHM values are nearly unchanged while the diffractions intensities of the (001) and (002) reflections are further reduced (compared to multilayer B). In the multilayer type D stack, the TiB_x layers grow with a preferred orientation. In the case of the NiAl phase, the x-ray diffraction patterns show diffraction reflections of the (110) and (211) lattice planes of the CsCl structured NiAl. A diffraction reflection of the (111) lattice plane is not observed anymore. The NiAl layers in multilayer type D are polycrystalline, and the diffraction intensities of the (110) oriented crystallites are the highest. The diffraction signals do not shift in their angular positions, and their FWHM values remain unchanged (compared to multilayer type C). This suggests that the nanoscale thin-film architecture has an impact on the growth and microstructure of both individual layer materials.

Figure 8 shows results of the TEM examination of a cross-sectional sample of a NiAl/TiB_x multilayer thin film of type A, deposited on a Si wafer substrate with 500 nm thick R.F. magnetron sputtered NiAl layers and 500 nm thick D.C. magnetron sputtered TiB_x layers. Figure 8(a) shows a STEM-HAADF image which corresponds via the mass contrast very well with a periodically stacked sequence of two-layer materials, NiAl and TiB_x. The NiAl layers appear bright due to higher mass compared with the dark TiB_x layers. The intended multilayer design can be recognized, i.e., the individual layers are well aligned, parallel to the substrate, and show only small deviations from a flat topography. Especially, the interfaces between the two layer materials (the phase boundaries) are sharp and pronounced. The BF image in Fig. 8(b) confirms this observation and reveals a columnar morphology for both layer materials. The columnar structure appears slightly coarser in the case of the NiAl layers. Nevertheless, both individual layer materials show a relatively dense and homogeneous structure. Some columns in both layers are tilted by a small angle versus the surface normal vector, while the majority of columns grow nearly perpendicular on

Published under an exclusive license by the AVS

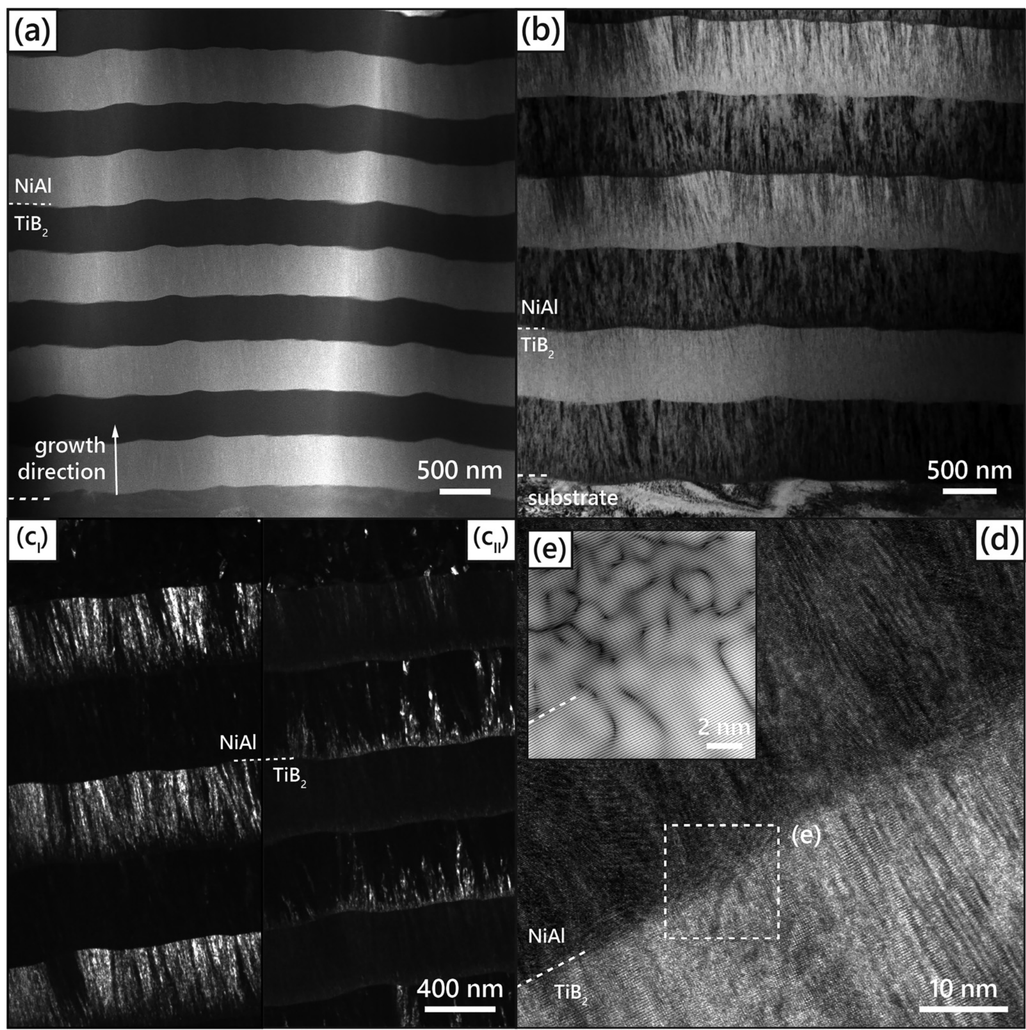

FIG. 8. TEM analysis of a NiAl/TiB_x multilayer thin film of type A according to the description in Table I, with 500 nm thick R.F. magnetron sputtered NiAl layers and 500 nm thick D.C. magnetron sputtered TiB_x layers on Si wafer substrates after cross-sectional TEM sample preparation: (a) STEM-HAADF image showing mass contrast resolution of the periodical stack of the individual layer materials, (b) BF image, (c) DF image, split into two parts C_I and C_{II}, referring to TiB_2 and NiAl related areas of the corresponding SAED patterns (not shown), (d) HRTEM image of an interface area between NiAl and TiB_x layers, and (e) IFFT image of the area marked in (d) by white dashed lines.

the layer beneath. One could even suggest seeing in each NiAl layer a transition zone of some 10 nm extension at the interfaces to the TiB_x layer beneath when the new condensing layer starts to grow with a finer columnar structure (which evolves with thickness to a coarser one). The DF images in Fig. 8(c) may support this observation; however, the evaluation of the images is not straightforward due to changes in the orientation of the crystallites in the growth direction, influencing the contrast situation. Figure 8(c) consists of two DF images, marked by C_I and C_{II}, respectively. The image C_I is related to an image of the TiB_x layers and reflects the more uniform alignment of the TiB_2 crystallites. This corresponds with the discussed textured growth of the TiB_x layers, and it is in good agreement with the TEM results shown in Fig. 6 for the R.F. magnetron sputtered TiB_x single layer thin films. The image C_{II} is related to an image of the NiAl layers and shows less bright crystallites, corresponding well with the growth of these layers in a polycrystalline structure without preferred orientation, as discussed above. Also, in this image, a small area at (and along) the interface can be seen, where the growth of these layers may be slightly different. This observation is becoming more clear and more visible with the HRTEM image shown in Fig. 8(d). Both layer materials are well crystallized at the interface area (which is shown by a white dashed line), and the lattice planes seem to cross over the interface, also suggesting a defined crystallographic orientation relation of the two

Published under an exclusive license by the AVS

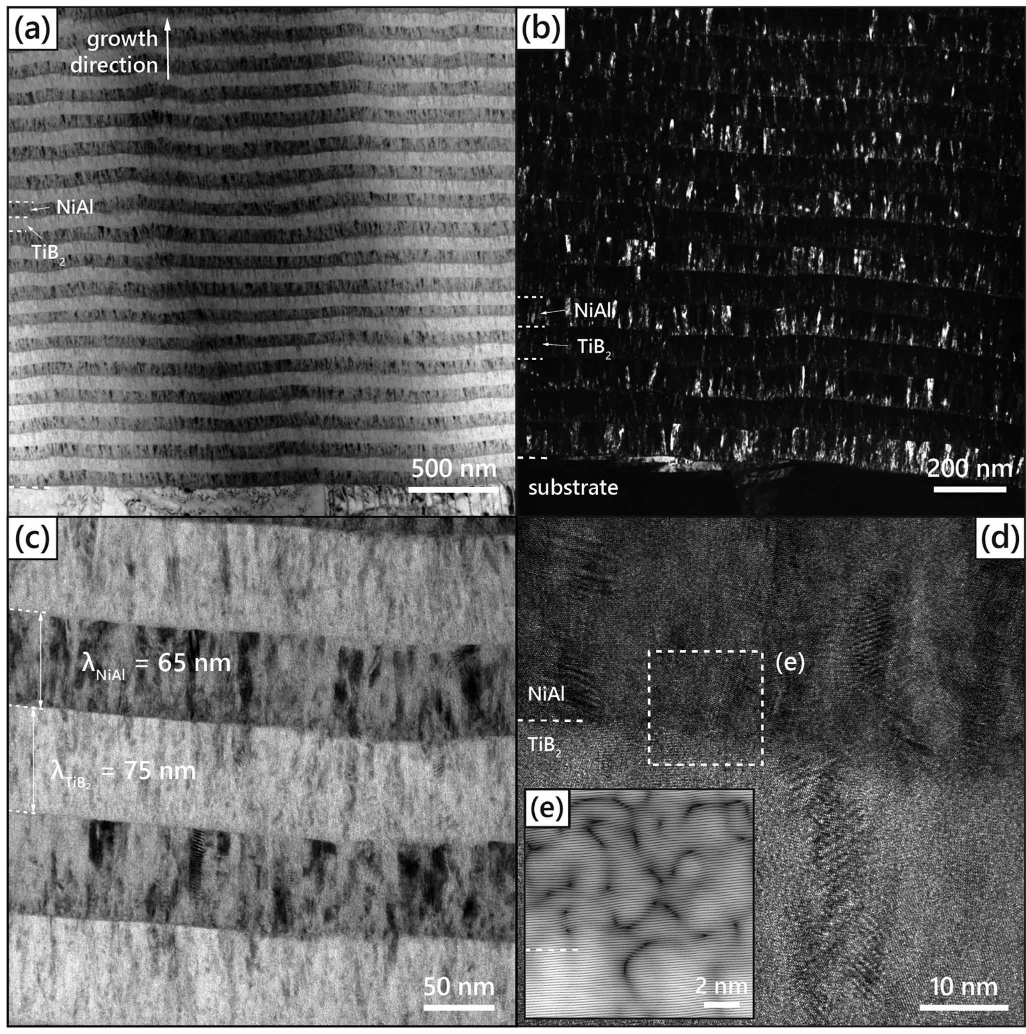

FIG. 9. TEM analysis of a NiAl/TiB_x multilayer thin film of type C according to the description in Table I, with 65 nm thick D.C. magnetron sputtered NiAl layers and 75 nm thick R.F. magnetron sputtered TiB_x layers on Si wafer substrates after cross-sectional TEM sample preparation: (a) BF image, (b) DF image, (c) BF image at a higher magnification than in (a), (d) HRTEM image of an interface area between NiAl and TiB_x layers, and (e) IFFT image of the area marked in (d) by white dashed lines.

layer materials at the phase boundaries. Figure 8(e) is an IFFT image of the area marked by white dashed lines in Fig. 8(d). The bright areas correspond to single columns, separated by the darker boundaries in this image. Qualitatively the TiB_x layer exhibits larger columns than the NiAl layer in this region. This fact might be a consequence of the growth direction and the usually smaller columns at the interface, becoming larger toward the top of the coating.

Results of the TEM investigation of a cross-sectional sample of a NiAl/TiB_x multilayer thin film type C on Si wafer substrate are presented in Fig. 9. This thin film has a nanoscale design with a bilayer period of 140 nm, and the two individual layers exhibit a very similar thickness, i.e., 65 nm for NiAl and 75 nm for TiB_x, respectively. The NiAl layers were D.C. magnetron sputtered, the TiB_x layers R.F. magnetron sputtered. The BF image in Fig. 9(a) shows a very homogeneous, periodical stacking sequence of the two layer materials NiAl (dark contrast) and TiB_x (bright contrast). This multilayer thin film is again grown without large microscale defects or voids, for example. The individual layers are well aligned to each other, parallel to the substrate surface, and show only locally some waviness. The interfaces between the two layer materials (the phase boundaries) seem to be sharp and pronounced. Both layer materials are grown in a columnar structure, and the columns in both layer materials show a relatively homogeneous tilting angle versus the surface normal vector (which may be associated at least to a larger part with the sample position in relation to the

Published under an exclusive license by the AVS

sputtering target during thin film deposition). Furthermore, the TiB_x layers' columnar morphology seems coarser in this multilayer thin film in comparison to that of the TiB_x layers in multilayer type A [see Fig. 8(b)]. At the same time, the columnar morphology of the NiAl layers in multilayer type C is not different from that in multilayer type A. The DF image in Fig. 9(b) significantly confirms the larger and less textured columns in the NiAl layers compared to the TiB_x layers. Figure 9(c) shows another BF image, at higher magnification, taken from another area of the multilayer thin film. This image contributes to all before-given statements, and it shows a very fine-scale structure of both layer materials. The structure of the TiB_x layers is smoother than that of the NiAl layers, and it is more homogeneous. This corresponds with the XRD results discussed above (Fig. 7), suggesting smaller crystallites for TiB_x layers but still a tendency to grow in a (001) oriented structure. The image of the NiAl layers is less homogeneous according to its polycrystalline structure. In all NiAl layers, one can observe an area around the interfaces to the TiB_x layers beneath, where the structure of the NiAl layers seems smoother than in the volume region of the layers. This area has a relatively constant extension over a distance of a few nanometers, and its nature should be related to the nucleation and growth of the new layer on the template layer below. Considering the dimensions of the unit cell of B2 CsCl structured NiAl phase with cubic lattice, this area may span over approximately 10 unit cells. Such an area of a slightly different structure is also visible in each TiB_x layer at (and along) the interface to the NiAl layers beneath (as indicated by a small area appearing with brighter contrast compared to the center region of the layers). This area shows an extension over a distance of a few nanometers from the interface again and would span over a few unit cells of the hexagonal structured TiB_2 phase with hexagonal lattice. In conclusion, the interface regions in this multilayer thin film of type C are similar or only slightly different in comparison with those in multilayer thin films of type A. This is supported by the HRTEM image in Fig. 9(d). This image reveals a very homogeneous, dense crystalline structure of the TiB_x layers with well-aligned lattice fringes and without disturbing grain boundary regions, as well, a dense, homogeneous polycrystalline structure of the NiAl layer. Both layer materials are well crystallized at the interface area (which is indicated again by a white dashed line), and some lattice fringes seem to cross over the interface, suggesting a defined crystallographic orientation relation of the two layer materials at the phase boundaries again. Figure 9(e) presents the IFFT image of the area marked by white dashed lines in Fig. 9(d). Like in the case of the multilayer type A with microscale dimensions, the TiB_x layer in this multilayer with nanoscale dimensions is well crystallized and only slightly strained, showing few dislocation lines. The NiAl layers orientation is locally well aligned with the TiB_x layer and exhibits more dark boundary regions since small columns start growing at the interface.

A closer insight into the thin films' chemical nature, especially at the interfaces of a NiAl/TiB_x multilayer of type C, is available via the combined EDX-EELS line scan shown in Fig. 10. This line scan shows the elemental composition and distribution over a few layers and reflects very well the main statements made before. It shows at first a very precise and periodical distribution of the major elements Ni, Al, Ti, and B. Especially, the interface regions are chemically

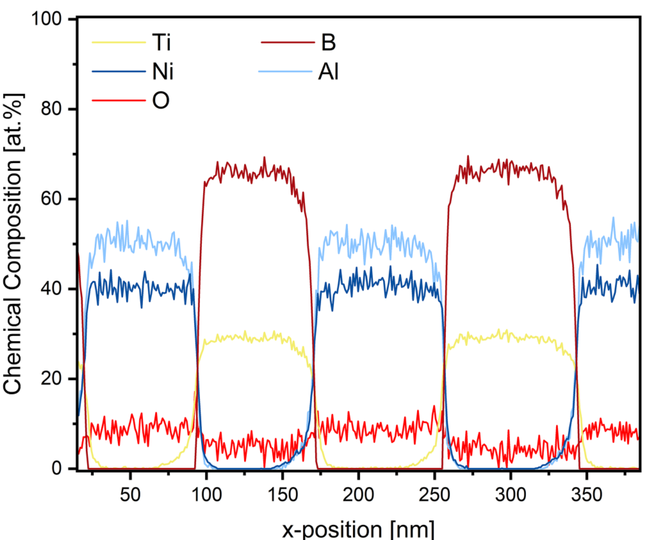

FIG. 10. Combined EDX-EELS line scan of the elemental composition and stacking sequence of a NiAl/TiB_x multilayer thin film of type C according to the description in Table I, with 65 nm thick D.C. magnetron sputtered NiAl layers and 75 nm thick R.F. magnetron sputtered TiB_x layers on Si wafer substrates (for preparation of these data please refer to Sec. II).

sharp as claimed for in the materials science-based and experimental approach of multilayer thin-film design and synthesis. Figure 10 shows further that the individual layers consist of their constituting elements only, i.e., a NiAl layer is composed of elements Ni and Al, and a TiB_x layer is composed of elements Ti and B. There is no cross-contamination of the layers by other elements and, therefore, no chemical disturbance of the individual layer structures. In conclusion, the above discussed structural effects observed at the interfaces of the multilayer thin films of both types A and C are not impacted by chemistry (and are then related to lattice plane orientations and variations in lattice parameters and lattice plane distances of the two layer materials according to their individual stoichiometries). Figure 10 further confirms the individual stoichiometry of the individual layer materials, corresponding closely with TiB_x and NiAl stoichiometry as discussed in the case of the respective single layer thin films (and measured by electron probe microanalysis). The relatively high oxygen content is caused by oxidation of the TEM sample and the poor accuracy of light elements' quantification EDX data due to the relatively poor X-ray yield of oxygen, overlapping edges in the low-energy region, complex background conditions, and theoretically determined k-factors as the quantification's base. The EELS quantification of oxygen was not satisfying because the features of the Ti-L edge were overlapping with the O-K edge.

Figure 11 collects the results of the TEM analyses of a cross-sectional sample of a NiAl/TiB_x multilayer thin film on Si wafer substrate of type D with a modified nanoscale architecture (i.e., the intermetallic layer NiAl is here thicker, 75 nm, than the TiB_x layer, 45 nm, while the bilayer period is very similar to that of the before

Published under an exclusive license by the AVS

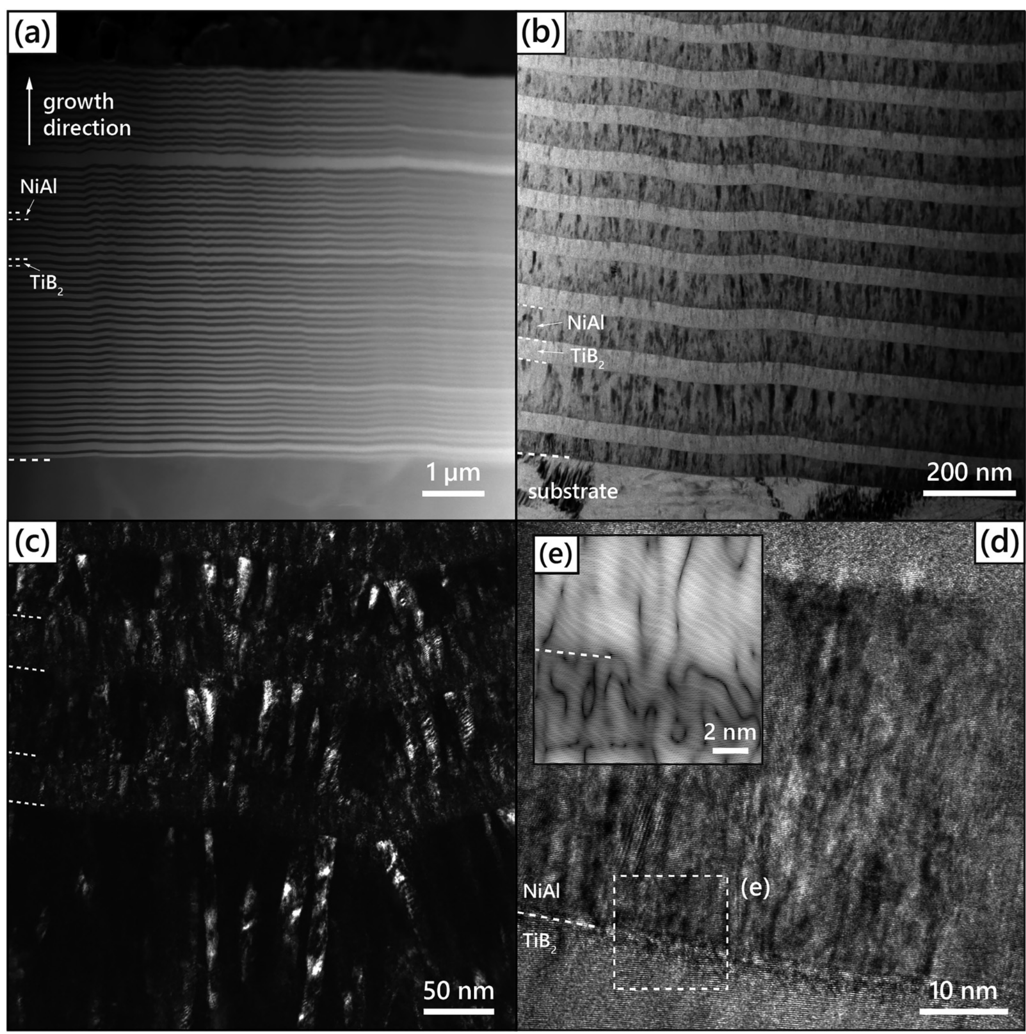

FIG. 11. TEM analysis of a NiAl/TiB_x multilayer thin film of type D according to the description in Table I, with 75 nm thick D.C. magnetron sputtered NiAl layers and 45 nm thick R.F. magnetron sputtered TiB_x layers on Si wafer substrates after cross-sectional TEM sample preparation: (a) STEM-HAADF image showing mass contrast resolution of the periodical stack of the individual layer materials, (b) BF image, (c) DF image, (d) HRTEM image of an interface area between NiAl and TiB_x layers, and (e) IFFT image of the area marked in (d) by white dashed lines.

discussed multilayer of type C, 120 nm). Again, the NiAl layers were D.C. magnetron sputtered, and the TiB_x layers R.F. magnetron sputtered. The STEM-HAADF image in Fig. 11(a) shows a pronounced mass contrast between the two different layer materials and confirms a periodically stacked sequence of both NiAl and TiB_x layers, both well aligned in parallel to the substrate and with only small, locally appearing waviness (please note that in the upper region of this multilayer thin film a local irregularity in the multilayer stack is visible, which we attribute to the experimental laboratory conditions when both the substrate table and the shutter are moved by hand, not automatized by a software steering, and has been forgotten during one step of the deposition process; however, this does not negatively affect the results presented here). The BF image in Fig. 11(b) shows again a very homogeneous, periodical stacking sequence of the two layer materials NiAl (dark contrast) and TiB_x (bright contrast), and no growth defects are visible at this length scale. Both layer materials grow in a columnar structure, which is more pronounced and coarser in the case of the NiAl layers, while that of the TiB_x layers appears smooth and more fine-scale. The nature of the interfaces (phase boundaries) is similar to that of the multilayers of type C (see Fig. 9): these are still relatively sharp and there is again an interface region with short extension at the interfaces of each layer, i.e., reflecting the early phases of nucleation and growth of a layer on the layer beneath. This can be seen for both NiAl and TiB_x layers. Furthermore, there seems to be some local disorder at the interfaces

Published under an exclusive license by the AVS

with some columnar grains extending into the subsequent layer. The DF image in Fig. 11(c) shows that the alignment of the grains is locally matching (in growth direction) between two adjacent layers, and locally not, and the columnar grains are even more randomly oriented within one layer (with respect to their tilting angle versus the surface normal vector). The interface region between a NiAl and a TiB_x layer is better visible in the HRTEM image in Fig. 11(d). It shows a homogeneous, dense crystalline structure of the TiB_x layers with well-aligned lattice fringes and without distorted grain boundary regions closer to the center region, while the region close to the interface to the NiAl layer is locally more distorted. The NiAl layer exhibits a polycrystalline structure with some more distorted regions. Generally, the interface area is more distorted locally in this multilayer of type D than compared to that of type C [see Fig. 9(d)]. This is also obvious in Fig. 11(e) in the IFFT image of the area marked by white dashed lines in Fig. 11(d). The dark contrast lines that can be interpreted as small-angle grain boundaries confirm that the columns in the NiAl layer are significantly larger than in the TiB_x layer. Similar to the multilayer structures with microscale and nanoscale dimensions discussed before, the TiB_x layer in this multilayer with nanoscale dimensions is well crystallized and moderately strained, showing few dislocation lines. The NiAl layer shows in this case more strained regions and more pronounced dislocation lines in a small area at the interface.

IV. SUMMARY AND CONCLUSIONS

This article presents the combination of a metallic hard material, TiB_x, and an intermetallic compound, NiAl, in a multilayer structure as a potential new approach for thin-film materials for engineering applications. Single layer NiAl and TiB_x, and NiAl/TiB_x multilayer thin films with a variation of the individual layer thickness and bilayer period were deposited by D.C. and R.F. magnetron sputtering. The impact of the operation mode of the sputtering targets on the microstructure of the thin films was investigated. The NiAl single layer thin films showed an operation mode-dependent growth in a polycrystalline structure with and without preferred orientation. Nearly stoichiometric, nanocrystalline, single-phase NiAl films were synthesized in a cubic B2 CsCl structure. The TiB_x single layer thin films exhibited an operation mode independent nanocrystalline, single-phase hexagonal structure with a pronounced (001) texture, a significant Ti-deficiency, and B-excess, resulting in stoichiometry in the range $TiB_{2.64}$–$TiB_{2.72}$. Both thin films microstructures were between zone 1 and zone T in the structure zone model of Thornton and were very homogeneous and dense. The existence of dislocations was revealed in both thin films materials. The microstructure of magnetron sputtered TiB_x thin films is described by the model of Mayrhofer *et al.*,[45] suggesting a crystalline TiB_2 phase surrounded by a B-rich grain boundary phase. The TiB_x thin films in this work exhibit a periodic stacking of both Ti- and B-planes orthogonal to the *c* axis of the TiB_2 lattice. However, the nature of the grain boundaries could not be resolved in full detail. Dislocation formation and structural ordering on the basis of stacking faults have only recently been described by Palisaitis *et al.* for slightly substoichiometric, epitaxial $TiB_{1.9}$ thin films of very high crystalline quality, synthesized by unbalanced magnetron sputtering at a substrate temperature of 900 °C.[83] The microstructure of the TiB_x thin films described here may be in between these two models of Mayrhofer *et al.* and Palisaitis *et al.* and is suggested to be described by a well-crystallized (001) oriented TiB_2 phase with fine-scale, small-angle grain boundaries. However, further insight into these issues would require additional TEM investigations, for example, plan-view TEM and high-resolution elemental composition analyses across the grain boundaries. In the multilayer stacks with modified microscale and nanoscale design, the TiB_x layers grew in a microstructure similar to that of the single layers with (001) texture, while the NiAl layers were polycrystalline without preferred orientation in microscale design and tended to grow in a polycrystalline structure with (211) preferred orientation in nanoscale designs. The dislocation densities at the NiAl/TiB_x phase boundaries changed with the multilayer design. In consequence, the volume fraction of the two layer materials, their column size, grain size, crystalline structure, and the nature of the interfaces have an impact on the dislocation density and ability to form dislocations in these NiAl/TiB_x-based multilayer structures (which should influence their deformation behavior and mechanical properties).

Multilayer thin films composed of nanocrystalline single layers can offer the possibility of combining an increase in strength with enhanced ductility and only low brittleness. The described NiAl/TiB_x multilayer thin films with relatively sharp interfaces accumulated dislocations in both the NiAl and the TiB_x layers. When the single layer thickness is reduced, the average columnar size can be selectively reduced because the growth phase after the nucleation phase is shortened. It was shown that the dislocation density at the interfaces is dependent on the design of the multilayers. Considering a nearly equal volume fraction of both materials, a nanoscale design (with a bilayer period of 140 nm, corresponding with the stacking of approximately 325 unit cells of NiAl and 230 unit cells of TiB_2 in each individual layer) seems to be favorable over a microscale design (with bilayer period of 1000 nm with the stacking of approximately 2500 unit cells of NiAl and 1500 unit cells of TiB_2 in each individual layer). Considering an unequal volume fraction, thin films with nano-design and thicker intermetallic layers (at nearly unchanged bilayer period, 120 nm, stacking of approximately 450 unit cells of NiAl and 125 unit cells of TiB_2 in each individual layer) seem to exhibit a more disturbed interface structure and larger dislocation density. This suggests that the volume, the volume fraction of the two layer materials (indicating the internal volume of grain boundaries) and the volume fraction of phase boundaries represent three tools to trigger the multilayer structure (and, thus, properties). Recently, Greczynski *et al.* have described a paradigm shift in physical vapor deposition by exploiting the huge potential of pulsed magnetron sputtering in HIPIMS processes, utilizing ionized species and their energy levels in a quite sophisticated way for the design of advanced thin films with tunable microstructure and properties.[22] This work suggests that conventional magnetron sputtering, and especially magnetron sputtering in R.F. mode, can as well be utilized to synthesize novel diboride thin films of high crystalline quality at low substrate temperature. It may be versatile to explore new PVD hybrid deposition methods in this regard by combining, for example, unbalanced D.C. magnetron sputtering with R.F. magnetron sputtering. The cross-sectional SEM images of the TiB_x layers grown with both

Published under an exclusive license by the AVS

D.C. and R.F. mode without external heating during deposition show dense structures and very smooth surfaces, different from what is known, for example, for magnetron sputtered transition metal nitride thin films. This could make such coatings interesting for future applications.

ACKNOWLEDGMENTS

The TEM investigations were carried out using facilities at the University Service Centre for Transmission Electron Microscopy, USTEM, TU Wien, Austria.

AUTHOR DECLARATIONS

Conflict of Interest

The authors have no conflicts to disclose.

DATA AVAILABILITY

The data that support the findings of this study are available from the corresponding author upon reasonable request.

REFERENCES

[1] A. Leyland and A. Matthews, Surf. Coat. Technol. **177–178**, 317 (2004).
[2] S. Zhang, D. Sun, Y. Fu, and H. Du, Surf. Coat. Technol. **198**, 2 (2005).
[3] A. A. Voevodin and J. S. Zabinski, Compos. Sci. Technol. **65**, 741 (2005).
[4] P. H. Mayrhofer, C. Mitterer, L. Hultman, and H. Clemens, Prog. Mater. Sci. **51**, 1032 (2006).
[5] S. Veprek and S. Reiprich, Thin Solid Films **268**, 64 (1995).
[6] U. Jansson, E. Lewin, M. Rasander, O. Eriksson, B. André, and U. Wiklund, Surf. Coat. Technol. **206**, 583 (2011).
[7] J. Musil, Surf. Coat. Technol. **207**, 50 (2012).
[8] U. Helmersson, S. Todorova, S. A. Barnett, J.-E. Sundgren, L. C. Markert, and J. E. Greene, J. Appl. Phys. **62**, 481 (1987).
[9] S. A. Barnett and M. Shinn, Ann. Rev. Mater. Sci. **24**, 481 (1994).
[10] P. C. Yashar and W. D. Sproul, Vacuum **55**, 179 (1999).
[11] M. Stueber, H. Holleck, H. Leiste, K. Seemann, S. Ulrich, and C. Ziebert, J. Alloys Compd. **483**, 321 (2009).
[12] C. M. Koller, R. Hollerweger, C. Sabitzer, R. Rachbauer, S. Kolozsvari, J. Paulitsch, and P. H. Mayrhofer, Surf. Coat. Technol. **259**, 599 (2014).
[13] R. Hauert and J. Patscheider, Adv. Eng. Mater. **2**, 247 (2000).
[14] H. Kindlund *et al.*, APL Mater. **1**, 042104 (2013).
[15] R. Daniel, M. Meindlhumer, J. Zalesak, W. Baumegger, J. Todt, T. Ziegelwanger, J. F. Keckes, C. Mitterer, and J. Keckes, Mater. Des. **196**, 109169 (2020).
[16] I. C. Schramm, M. P. Johansson Joesaar, J. Jensen, F. Mücklich, and M. Odén, Acta Mater. **119**, 218 (2016).
[17] S. M. Aouadi, J. Gu, and D. Berman, J. Vac. Sci. Technol. A **38**, 050802 (2020).
[18] I. Petrov, P. B. Barna, L. Hultman, and J. E. Greene, J. Vac. Sci. Technol. A **21**, S117 (2003).
[19] D. G. Sangiovanni, V. Chirita, and L. Hultman, Thin Solid Films **520**, 4080 (2012).
[20] K. Balasubramanian, S. V. Khare, and D. Gall, Acta Mater. **152**, 175 (2018).
[21] S. Liu, K. Chang, S. Mráz, X. Chen, M. Hans, D. Music, D. Primetzhofer, and J. M. Schneider, Acta Mater. **165**, 615 (2019).
[22] G. Greczynski, I. Petrov, J. E. Greene, and L. Hultman, J. Vac. Sci. Technol. A **37**, 060801 (2019).
[23] C. M. Ward-Close, R. Minor, and P. J. Doorbar, Intermetallics **4**, 217 (1996).
[24] S. Suresh, N. Shenbag, and V. Moorthi, Proc. Eng. **38**, 89 (2012).
[25] H. Zhang, H. Zhu, J. Huang, J. Li, and Z. Xie, Mater. Sci. Eng. A **719**, 140 (2018).
[26] D. B. Miracle, Acta Metall. Mater. **41**, 649 (1993).
[27] R. Darolia, J. Mater. **43**, 44 (1991).
[28] R. D. Noebe, R. R. Bowman, and M. V. Nathal, "Review of the physical and mechanical properties and potential applications of the B2 compound NiAl," NASA Technical Memorandum 105598, 1992.
[29] I. Ansara, N. Dupin, H. L. Lukas, and B. Sundman, J. Alloys Compd. **247**, 20 (1997).
[30] Y. Ding, Y. Zhang, D. O. Northwood, and A. T. Alpas, Surf. Coat. Technol. **94–95**, 483 (1997).
[31] P. de Almeida, R. Schäublin, A. Almazouzi, M. Victoria, and F. Levy, Thin Solid Films **368**, 26 (2000).
[32] M. A. Bestor, R. L. Martens, R. A. Holler, and M. L. Weaver, Intermetallics **18**, 2159 (2010).
[33] J. A. Howell, S. E. Mohney, and C. L. Muhlstein, J. Vac. Sci. Technol. B **29**, 042002 (2011).
[34] D.-C. Tian and X.-B. Wang, J. Phys. Condens. Matter **4**, 8765 (1992).
[35] R. G. Munro, J. Res. Natl. Inst. Stand. Technol. **105**, 709 (2000).
[36] H. Chen and X. Zhou, Chem. Front. **7**, 2248 (2020).
[37] X. Ma, C. Li, Z. Du, and W. Zhang, J. Alloys Compd. **370**, 149 (2004).
[38] H. O. Pierson and A. W. Mullendore, Thin Solid Films **95**, 99 (1982).
[39] H. Karner, J. Laimer, H. Störi, and P. Rödhammer, Surf. Coat. Technol. **39–40**, 293 (1989).
[40] J. F. Pierson, T. Belmonte, T. Czerwiec, D. Hertz, and H. Michel, Thin Solid Films **359**, 68 (2000).
[41] S. Jayaraman, E. J. Klein, Y. Yang, D. Y. Kim, G. S. Girolami, and J. R. Abelson, J. Vac. Sci. Technol. A **23**, 631 (2005).
[42] D. P. Gruber *et al.*, Surf. Coat. Technol. **399**, 126181 (2020).
[43] J.-E. Sundgren and H. T. G. Hentzell, J. Vac. Sci. Technol. A **4**, 2259 (1986).
[44] C. Mitterer, J. Solid State Chem. **133**, 279 (1997).
[45] P. H. Mayrhofer, C. Mitterer, J. G. Wen, J. E. Greene, and I. Petrov, Appl. Phys. Lett. **86**, 131909 (2005).
[46] I. Petrov *et al.*, J. Vac. Sci. Technol. A **35**, 050601 (2017).
[47] J. P. Riviere, Ph. Guesdon, J. Delafond, M. F. Denanot, G. Farges, and D. Degout, Thin Solid Films **204**, 151 (1991).
[48] M. Berger, L. Karlsson, M. Larsson, and S. Hogmark, Thin Solid Films **401**, 179 (2001).
[49] M. Audronis, A. Leyland, P. J. Kelly, and A. Matthews, Surf. Coat. Technol. **201**, 3970 (2006).
[50] J. Neidhardt, S. Mráz, J. M. Schneider, E. Strub, W. Bohne, B. Liedke, W. Möller, and C. Mitterer, J. Appl. Phys. **104**, 063304 (2008).
[51] N. Nedfors, D. Primetzhofer, I. Zhirkov, J. Palisaitis, P. O. A. Persson, J. E. Greene, I. Patrov, and J. Rosen, Vacuum **177**, 109355 (2020).
[52] I. Zhirkov, A. Petruhins, L.-A. Naslund, S. Kolozsvári, P. Polcik, and J. Rosen, Appl. Phys. Lett. **107**, 184103 (2015).
[53] P. A. Dearnley and T. Bell, Surf. Eng. **1**, 203 (1985).
[54] M. Audronis, A. Leyland, A. Matthews, J. G. Wen, and I. Petrov, Acta Mater. **56**, 4172 (2008).
[55] C.-H. Cheng, J.-W. Lee, L.-W. Ho, H.-W. Chen, Y.-C. Chan, and J.-G. Duh, Surf. Coat. Technol. **206**, 1711 (2011).
[56] F. Ge, C. Chen, R. Shu, F. Meng, P. Li, and F. Huang, Vacuum **135**, 66 (2017).
[57] M. Samuelsson, J. Jensen, U. Helmersson, L. Hultman, and H. Högberg, Thin Solid Films **526**, 163 (2012).
[58] N. Nedfors, A. Mockute, J. Palisaitis, P. O. Å. Persson, L.-Å. Näslund, and J. Rosen, Surf. Coat. Technol. **304**, 203 (2016).
[59] B. Bakhit, I. Petrov, J. E. Greene, L. Hultman, J. Rosén, and G. Greczynski, J. Vac. Sci. Technol. A **36**, 030604 (2018).
[60] N. Nedfors, O. Vozniy, and J. Rosen, J. Vac. Sci. Technol. A **36**, 031510 (2018).
[61] N. Hellgren, J. Thörnberg, I. Zhirkov, M. A. Sortica, I. Petrov, J. E. Greene, L. Hultman, and J. Rosen, Vacuum **169**, 108884 (2019).
[62] B. Bakhit, D. L. J. Engberg, J. Lu, J. Rosen, H. Högberg, L. Hultman, I. Petrov, J. E. Greene, and G. Greczynski, J. Vac. Sci. Technol. A **37**, 031506 (2019).

Published under an exclusive license by the AVS

[63]J. Thörnberg, B. Bakhit, J. Palisaitis, N. Hellgren, L. Hultman, G. Greczynski, P. O. Å. Persson, I. Petrov, and J. Rosen, Surf. Coat. Technol. **420**, 127353 (2021).
[64]N. Kalfagiannis, G. Volonakis, L. Tsetseris, and S. Logothetidis, J. Phys. D: Appl. Phys. **44**, 385402 (2011).
[65]M. Dahlqvist, U. Jansson, and J. Rosen, J. Phys. Condens. Matter **27**, 435702 (2015).
[66]B. Alling, H. Högberg, R. Armiento, J. Rosen, and L. Hultman, Sci. Rep. **5**, 09888 (2015).
[67]H. Euchner and P. H. Mayrhofer, Thin Solid Films **583**, 46 (2015).
[68]C. Rebholz, A. Leyland, J. M. Schneider, A. A. Voevodin, and A. Matthews, Surf. Coat. Technol. **120–121**, 412 (1999).
[69]A. Mockute *et al.*, Scr. Mater. **127**, 122 (2017).
[70]P. Bliem, S. Mráz, S. Sen, O. Hunold, and J. M. Schneider, Sci. Rep. **8**, 15570 (2018).
[71]R. Hahn, V. Moraes, A. Limbeck, P. Polcik, P. H. Mayrhofer, and H. Euchner, Acta Mater. **174**, 398 (2019).
[72]M. Stüber, H. Riedl, T. Wojcik, S. Ulrich, H. Leiste, and P. H. Mayrhofer, Thin Solid Films **688**, 137361 (2019).
[73]B. Bakhit, J. Palisaitis, J. Thörnberg, J. Rosen, P. O. A. Persson, L. Hultman, I. Petrov, J. E. Greene, and G. Greczynski, Acta Mater. **196**, 677 (2020).
[74]O. V. Sobol, S. N. Dub, A. D. Pogrebnjak, R. P. Mygushchenko, A. A. Postelnyk, A. V. Zvyagolsky, and G. N. Tolmachova, Thin Solid Films **662**, 137 (2018).
[75]B. Grančič *et al.*, Surf. Coat. Technol. **367**, 341 (2019).
[76]C. Fuger, V. Moraes, R. Hahn, H. Bolvardi, P. Polcik, H. Riedl, and P. H. Mayrhofer, MRS Commun. **9**, 375 (2019).
[77]R. Psiuk, M. Milczarek, P. Jenczyk, P. Denis, D. M. Jarząbek, P. Bazarnik, M. Pisarek, and T. Móscicki, Appl. Surf. Sci. **570**, 151239 (2021).
[78]V. Moraes, H. Riedl, C. Fuger, P. Polcik, H. Bolvardi, D. Holec, and P. H. Mayrhofer, Sci. Rep. **8**, 9288 (2018).
[79]A. Kirnbauer, A. Wagner, V. Moraes, D. Primetzhofer, M. Hans, J. M. Schneider, P. Polcik, and P. H. Mayrhofer, Acta Mater. **200**, 559 (2020).
[80]B. Bakhit, J. Palisaitis, P. O. Å. Persson, B. Alling, J. Rosen, L. Hultman, I. Petrov, J. E. Greene, and G. Greczynski, Surf. Coat. Technol. **401**, 126237 (2020).
[81]M. Magnuson, L. Hultman, and H. Högberg, Vacuum **196**, 110567 (2022).
[82]J. T. Gudmundsson, N. Brenning, D. Lundin, and U. Helmersson, J. Vac. Sci. Technol. A **30**, 030801 (2012).
[83]J. Palisaitis *et al.*, Acta Mater. **204**, 116510 (2021).
[84]H. Holleck and H. Schulz, Surf. Coat. Technol. **36**, 707 (1988).
[85]K. W. Lee, Y.-H. Chen, Y.-W. Chung, and L. M. Keer, Surf. Coat. Technol. **177–178**, 591 (2004).
[86]D. J. Li, J. Yang, X. H. Zhang, and M. Cao, J. Vac. Sci. Technol. B **25**, L11 (2007).
[87]M. S. Wong and Y. C. Lee, Surf. Coat. Technol. **120–121**, 194 (1999).
[88]Y. D. Sun *et al.*, Surf. Coat. Technol. **228**, S385 (2013).
[89]J. Rao, A. Sharma, and T. Rose, Coatings **8**, 12 (2018).
[90]Y. B. Kang, D. J. Li, H. Y. Wang, J. Y. Yan, S. Zhang, and X. Y. Deng, Appl. Surf. Sci. **258**, 2206 (2012).
[91]C. Kainz, N. Schalk, M. Tkadletz, C. Mitterer, and C. Czettl, Surf. Coat. Technol. **370**, 311 (2019).
[92]R. Gilmore, M. A. Baker, P. N. Gibson, and W. Gissler, Surf. Coat. Technol. **116–119**, 1127 (1999).
[93]J. Rao, R. Cruz, K. J. Lawson, and J. R. Nicholls, Diam. Relat. Mater. **14**, 1805 (2005).
[94]L. Dong *et al.*, Thin Solid Films **520**, 5328 (2012).
[95]L. Dong, Y. D. Sun, and D. J. Li, Surf. Coat. Technol. **205**, S422 (2010).
[96]D. Mao, Y. Xu, L. Dong, J. Wu, M. Zhao, and D. Li, Coatings **9**, 600 (2019).
[97]A. Twardowska, A. Kopia, and P. Malczewski, Coatings **10**, 621 (2020).
[98]M. F. Vales Silva and J. R. Nicholls, Surf. Coat. Technol. **142–144**, 934 (2001).
[99]M. Berger and M. Larsson, Surf. Eng. **16**, 122 (2000).
[100]K. Chu, Y. H. Lu, and Y. G. Shen, Thin Solid Films **516**, 5313 (2008).
[101]G. Zhao, J. Wang, Y. Deng, T. Yan, W. Liang, T. Li, L. Zhang, Q. Jia, and Y. Wan, J. Mater. Res. Technol. **16**, 290 (2022).
[102]P. Sejč, P. Jaško, P. Baksa, and J. Belanová, Manuf. Technol. **17**, 570 (2017).
[103]A. Kohns, K. Ortner, and T. Jung, Adv. Eng. Mater. **11**, 67 (2009).
[104]C. Wang, J. Han, J. M. Pureza, and Y.-W. Chung, Surf. Coat. Technol. **237**, 158 (2013).
[105]C. Wang, K. Shi, C. Gross, J. M. Pureza, M. de Mesquita Lacerda, and Y.-W. Chung, Surf. Coat. Technol. **257**, 206 (2014).
[106]M. Stüber, V. Schier, and H. Holleck, Surf. Coat. Technol. **74–75**, 833 (1995).
[107]J. Ye, S. Ulrich, K. Sell, H. Leiste, M. Stüber, and H. Holleck, Surf. Coat. Technol. **174–175**, 959 (2003).
[108]A. Kratzsch, S. Ulrich, H. Leiste, M. Stüber, and H. Holleck, Surf. Coat. Technol. **116–119**, 949 (1999).
[109]J. A. Thornton, J. Vac. Sci. Technol. A **4**, 3059 (1986).
[110]B. Ning, M. Shamsuzzola, and M. L. Weaver, Surf. Coat. Technol. **179**, 201 (2004).
[111]C. M. T. Sanchez, B. Rebollo Plata, M. E. H. Maia da Costa, and F. L. Freire, Jr., Surf. Coat. Technol. **205**, 3698 (2011).
[112]E. Kelesoglu and C. Mitterer, Surf. Coat. Technol. **98**, 1483 (1998).
[113]M. Berger, E. Coronel, and E. Olsson, Surf. Coat. Technol. **185**, 240 (2004).

Published under an exclusive license by the AVS